



JGR Atmospheres

RESEARCH ARTICLE

10.1029/2018JD030189

Key Points:

- Radiative transfer calculations suggest that Arctic stratocumuli can form naturally through clear-sky radiative cooling during all seasons
- Properties of Arctic stratocumuli that form by radiative cooling are sensitive to the characteristics of the environment in which they form
- These sensitivities might have important implications for the Arctic climate

Supporting Information:

- Supporting Information S1

Correspondence to:

L. F. Simpfendoerfer,
lfs5089@gmail.com

Citation:

Simpfendoerfer, L. F., Verlinde, J., Harrington, J. Y., Shupe, M. D., Chen, Y.-S., Clothiaux, E. E., & Golaz, J.-C. (2019). Formation of Arctic stratocumuli through atmospheric radiative cooling. *Journal of Geophysical Research: Atmospheres*, 124, 9644–9664. <https://doi.org/10.1029/2018JD030189>

Received 18 DEC 2018

Accepted 8 JUL 2019

Accepted article online 16 JUL 2019

Published online 27 AUG 2019

Author Contributions:

Conceptualization: Johannes Verlinde, Jerry Y. Harrington, Matthew D. Shupe, Yao-Sheng Chen, Eugene E. Clothiaux

Formal analysis: Johannes Verlinde

Funding acquisition: Johannes Verlinde

Methodology: Johannes Verlinde, Jerry Y. Harrington, Matthew D. Shupe, Yao-Sheng Chen, Eugene E. Clothiaux

Resources: Johannes Verlinde, Jerry Y. Harrington

Software: Jerry Y. Harrington, Jean-Christophe Golaz

Supervision: Johannes Verlinde, Jerry Y. Harrington, Matthew D. Shupe, Yao-Sheng Chen, Eugene E. Clothiaux

Writing – review & editing: Johannes Verlinde, Jerry Y. Harrington, Matthew (continued)

©2019. American Geophysical Union.
All Rights Reserved.

Formation of Arctic Stratocumuli Through Atmospheric Radiative Cooling

Lucien F. Simpfendoerfer¹ , Johannes Verlinde¹ , Jerry Y. Harrington¹, Matthew D. Shupe² , Yao-Sheng Chen^{1,3} , Eugene E. Clothiaux¹ , and Jean-Christophe Golaz⁴

¹Department of Meteorology and Atmospheric Science, Pennsylvania State University, PA, USA, ²Cooperative Institute for Research in Environmental Sciences, University of Colorado and NOAA-Earth System Research Laboratory, Boulder, CO, USA, ³Now at Cooperative Institute for Research in Environmental Sciences, University of Colorado and NOAA-Earth System Research Laboratory, Boulder, CO, USA, ⁴Lawrence Livermore National Laboratory, Livermore, CA, USA

Abstract Stratocumulus clouds are important to the Arctic climate because they are prevalent and exert a strong radiative forcing on the surface. However, relatively little is known about how stratocumulus clouds form in the Arctic. In this study, radiative transfer calculations are used to show that the timescale over which stably stratified Arctic temperature and water vapor profiles cool to saturation is less than typical residence times for individual air parcels in the Arctic. This result is consistent with previous studies in suggesting that elevated stratocumulus can form naturally through clear-sky radiative cooling during all seasons, without assistance from frontal lifting or other atmospheric forcing. Single column model simulations of the cloud formation process, after radiative cooling has resulted in saturation in a stably stratified profile, suggest that stratocumulus cloud properties are sensitive to the characteristics of the environment in which the formation process takes place. For example, sensitivity tests suggest that clouds may attain liquid water paths of over 50 g/m² if they form in moist environments but may become locked in a low-liquid water path quasi steady state or dissipate within hours if they form in dry environments. A potential consequence of these sensitivities is that when an Arctic stratocumulus layer forms by radiative cooling, it is more likely to become optically thick, optically thin, or dissipate than it is to obtain an intermediate optical thickness. This could help explain why the cloudy and radiatively clear atmospheric states are so prevalent across the Arctic.

Plain Language Summary While Arctic stratocumulus cloud layers play a strong role in the Arctic climate and may be contributing to rapid Arctic climate change, relatively little research has focused on how the cloud layers form. In this study, we found that Arctic stratocumulus cloud layers can form naturally as the Arctic atmosphere cools through radiative emission, confirming results from previous studies. This may help explain why the stratocumulus cloud layers are so prevalent across the Arctic. We also found that the properties of stratocumulus layers that form through radiative cooling are sensitive to characteristics of the environment in which the formation process takes place. A potential consequence of these sensitivities is that cloud layers that form by this mechanism are more likely to contain large or small amounts of liquid than intermediate amounts of liquid. This might help explain a key characteristic of the Arctic climate: That the atmosphere is more likely to emit large or small amounts of infrared radiation than intermediate amounts of infrared radiation toward the surface.

1. Introduction

Arctic surface temperatures are increasing more than twice as rapidly as those in the midlatitudes through a process known as Arctic amplification (Overland et al., 2014). Arctic amplification is impacting Arctic terrestrial, freshwater, and marine ecosystems at rates that may outpace the ecosystems' abilities to adapt and is threatening food security and ways of life in indigenous and other communities across the Arctic (Larsen et al., 2014). Arctic amplification is also relaxing the equator-to-pole temperature gradient, which may change midlatitude storm tracks, slow the progression of midlatitude weather patterns, and consequently alter midlatitude climate (Cohen et al., 2014). Studies have shown that wintertime Arctic amplification is primarily caused by an increase in downwelling longwave radiation (DLR) at the surface (Gong et al., 2017; Lee et al., 2017; Lu & Cai, 2010; Vavrus, 2004).

D. Shupe, Yao-Sheng Chen, Eugene E. Clothiaux, Jean-Christophe Golaz

Clouds are a primary source of DLR in the Arctic. When optically thick clouds are present, the DLR is typically much larger than when skies are clear. This results in a distribution of the net longwave irradiance at the surface that is bimodal in winter (Shupe & Intrieri, 2004; Stramler et al., 2011) and raises the possibility that changes in the presence of optically thick clouds might be contributing to Arctic amplification. However, in order to understand and predict changes in this contribution, it is important first to understand how optically thick clouds form, persist, and dissipate across the Arctic.

Stratocumulus is a dominant cloud type in the Arctic. Arctic stratocumuli may be composed of only liquid or a mixture of liquid and ice, exist in broad sheets, and can persist for up to several days (Curry et al., 1988; Intrieri et al., 2002; Morrison et al., 2011; Shupe et al., 2006, 2011; Sotiropoulou et al., 2014). They typically have lapse rates close to the moist adiabatic lapse rate and exist within turbulent mixed layers that are either dynamically coupled to or decoupled from the surface (Curry et al., 1988; Shupe et al., 2013; Sedlar & Shupe, 2014; Sotiropoulou et al., 2014; Brooks et al., 2017). Arctic stratocumuli play a key role in the Arctic climate because they are often optically thick and are present for up to 30% of the year, depending on location (Bennartz et al., 2013; Shupe et al., 2011). While Arctic stratocumuli have been studied extensively in recent decades, a majority of research has focused on why the stratocumuli persist for such long periods of time; relatively little research has focused on how they form.

Thus far, several formation mechanisms have been proposed. First, Arctic stratocumuli may form through the cooling, moistening, or growth of atmospheric boundary layers that are maintained through surface fluxes (Harrington & Olsson, 2001a; Klein et al., 2009; Pithan et al., 2018). While this formation mechanism may be dominant over open water during cold air outbreaks, it is unlikely to be dominant over land or the pack ice where surface fluxes are small (Persson et al., 2002). Second, stratocumuli may form from surface fogs. Surface fogs develop when the Arctic atmospheric boundary layer cools through turbulent fluxes and radiative processes. The fog may develop a turbulent mixed layer if the atmosphere above is cloud free, which permits the fog to gradually lift through entrainment and transform into an Arctic stratocumulus cloud (Curry, 1983; Cronin & Tziperman, 2015; Herman & Goody, 1976; Pithan et al., 2018; Tjernström et al., 2015).

Finally, Arctic stratocumuli may form through the radiative cooling of cloud-free, moist atmospheric layers. Elevated layers of moisture may originate from leads, polynyas, or the midlatitudes and are commonly observed across the Arctic (Devasthale et al., 2011; Nygård et al., 2014). Once in the Arctic, these moist layers may drift across the Arctic for long periods of time, cooling continuously through radiative emission. Previous modeling studies have shown that when such a layer cools to its dew point temperature, a tenuous liquid cloud forms. The cloud then deepens through a positive feedback between radiative cooling and condensation, eventually becoming a mature stratocumulus cloud layer (Curry & Herman, 1985; Garrett et al., 2009; McInnes & Curry, 1995; Zhang, 1999). This formation process is similar to the formation process outlined by Herman and Goody (1976), who showed that elevated liquid phase stratiform clouds can form through radiative cooling in a stably stratified atmosphere. This formation process will be hereafter referred to as “formation by radiative cooling.”

In the first portion of this study, a radiative transfer model is used to characterize the timescale over which stably stratified, Arctic atmospheric profiles cool to saturation through only radiative processes. This enables us to determine if radiative cooling is capable of driving Arctic stratocumulus formation in stable atmospheric layers, without help from synoptic/mesoscale forcing or turbulent processes. Next, a single column model (SCM) with idealized representations of radiative, turbulent, and microphysical processes is used to determine how the formation process is sensitive to various environmental characteristics. This second portion of the study is meant to broadly explore a parameter space that could help explain important characteristics of the Arctic climate but which has not yet been explored in the literature. Due to the simplified nature of the SCM, the parameter space exploration should not be viewed as exhaustive; instead, it should be used to inform more directed studies with more sophisticated modeling tools.

2. Clear-Sky Cooling Process

In this section, a radiative transfer model and clear-sky radiosonde observations from near Utqiagvik (formerly called Barrow), Alaska, are used to estimate the timescale over which Arctic atmospheric profiles cool to saturation through radiative processes. The calculations assume that only radiative processes affect the

profiles' thermodynamic properties. While this assumption is not necessarily valid in the Arctic atmosphere, these calculations help determine whether clear-sky radiative cooling can drive Arctic stratocumulus formation in moist atmospheric layers, without help from other processes. The radiative transfer calculations are also used to examine the effectiveness of local heating processes, such as solar heating and subsidence, in inhibiting cloud formation by radiative cooling.

2.1. Identification of Clear-Sky Profiles and Simulation of Radiative Cooling

Profiles observed by all 3,369 radiosondes launched between 1 January 2012 and 31 December 2015 from the Department of Energy Atmospheric Radiation Measurement (ARM) Program observatory at the North Slope of Alaska (NSA), which is located near Utqiagvik, AK (71.323°N, 156.609°W), were considered in the analysis (ARM User Facility, 1993). A combination of the Department of Energy ARM Ka-band zenith pointing radar signal-to-noise ratios (ARM User Facility, 1990a) and a micropulse lidar cloud mask (ARM User Facility, 1990b; Wang & Sassen, 2001) was used to determine whether liquid cloud layers or plumes of ice precipitation were present above 250 m around the time of each launch. If no liquid layers or plumes of ice precipitation appeared in either instrument's observations within (plus or minus) 15 min of the radiosonde launch below 4,000 m, 30 min of the radiosonde launch between 4,000 and 8,000 m, and 60 min of the launch above 8,000 m, the launch was marked as "clear sky" and considered for further analysis of the radiative cooling process. A lower height limit of 250 m was chosen to increase the sample size of radiosonde observations; hydrometeors below 250 m are unlikely to severely affect radiative heating rates above, except in cases when opaque fogs form within strong surface-based temperature inversions. The observational intervals of 30, 60, and 120 min were chosen to provide a large sample of the atmospheric conditions above the NSA observatory at the time of each launch and minimize the probability that each radiosonde encountered undetected hydrometeors during its ascent.

In all, 418 of the 3,369 radiosondes launched at the NSA observatory were marked as clear sky. Fifty-one percent of these clear-sky launches occurred in winter (Dec–Mar), 16% in spring (Apr–May), 21% in summer (Jun–Aug), and 12% in autumn (Sept–Nov).

Each of the clear-sky radiosonde profiles was cooled to saturation using the Rapid Radiative Transfer Model (RRTM; Mlawer et al., 1997; Mlawer & Clough, 1997). Longwave and shortwave heating rates were calculated and applied iteratively with a time step of 60 min for a total of 14 days or until the radiosonde profile saturated above 250 m (lowest height checked for hydrometeors). The calculations were initialized with the profiles of temperature (T), water vapor mixing ratio (r_v), and pressure (p) measured by radiosonde. The radiosonde profiles were supplemented above 20 km by values from the default sub-Arctic winter sounding provided by RRTM. The profile of CO₂ was assumed to be well mixed with a uniform concentration of 400 ppm, while the profiles of O₃, N₂O, CH₄, O₂, and CO were initialized with values from the RRTM default sub-Arctic winter sounding. No liquid or ice condensate was included in the radiative transfer calculations. Although aerosol particles do influence radiative transfer in the Arctic atmosphere, they were excluded from these calculations to isolate the role thermodynamic profiles play in the clear-sky radiative cooling process.

Longwave calculations were performed with eight streams and at vertical resolutions of 25 m below 5,000 m, 200 m between 5,000 and 20,000 m, and 2,000 m above 20,000 m. Shortwave calculations were performed with 16 streams and at vertical resolutions of 50 m below 5,000 m, 200 m between 5,000 and 20,000 m, and 2,000 m above 20,000 m. At each time step, the solar zenith angle was updated using ephemeris calculations (Wilson, 1980) for the NSA observatory and the surface temperature was set to the temperature in the lowest atmospheric grid box. After heating rates from each radiative transfer calculation were applied, static instabilities were removed using a simple dry-air convective adjustment scheme. Sensitivity tests indicate that the evolutions of profiles cooled with the radiative transfer model were insensitive to reductions in the vertical grid spacing or time step of the radiative transfer calculations.

Figure 1 illustrates the simulated cooling process for two atmospheric profiles observed by radiosonde at the NSA observatory. The profile observed on 14 January 2014 saturates at 575 m after 43 hr of cooling, while the profile observed on 13 February 2015 first saturates at 1,450 m after 42 hr of cooling, leading hypothetically to the formation of Arctic stratocumulus cloud layers. In both profiles, cooling occurs most rapidly near the absolute maxima in T and dew point temperature.

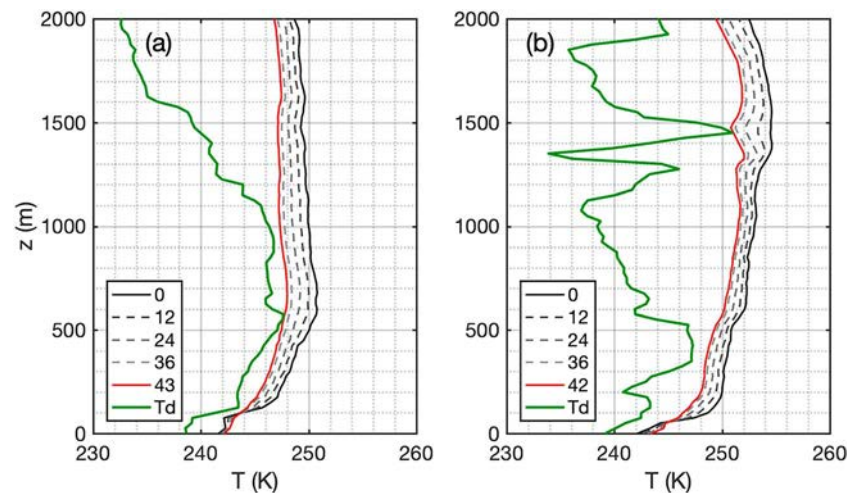


Figure 1. Illustrations of the clear-sky radiative cooling process for atmospheric profiles observed by radiosondes launched from the North Slope of Alaska observatory at (a) 5:30 UTC on 14 January 2014 and (b) 17:30 UTC on 13 February 2015. The solid black lines show the initial temperature profiles, while the green lines show the initial dew point profiles. The dashed lines show profiles of temperature at 12-hr intervals of cooling (hours of cooling shown in the legend). The solid red lines show the temperature profile when the atmosphere reaches liquid saturation (number of hours required to saturate is shown in the legend).

2.2. Results and Discussion of Radiative Transfer Calculations

All 418 clear-sky profiles examined in this study saturated within 2 weeks of radiative cooling. Of the 418 profiles, 131 first saturated above 2,500 m and 43 saturated from low levels upward, eventually saturating at the 250-m level. The remaining 244 profiles first saturated between 250 and 2,500 m and are the most likely to have produced elevated Arctic stratocumulus cloud layers. The heights at which these 244 profiles first saturated are distributed as in Figure 2a. Analysis in the remainder of this section will focus on these 244 profiles, which are hereafter referred to as *stratocumulus-forming profiles*.

The distributions of the timescale over which saturation occurs (the “cloud formation timescale”) imply that radiative cooling is capable of driving the formation of Arctic stratocumulus clouds in stably stratified layers. For radiative cooling to drive cloud formation, the cloud formation timescale must frequently be shorter than the average residence time for air parcels in the Arctic. Such a difference in timescales would permit parcels in many of the stratocumulus-forming profiles to saturate before leaving the Arctic, forming clouds. According to the radiative transfer calculations in this section, the saturation timescale is indeed less than the average residence time: the median saturation times during winter, spring, summer, and fall are 1.7, 2.4, 3.5, and 2.1 days, respectively (Figure 2b). These values are comparable to the formation timescales in previous simulations (Garrett et al., 2009; Herman & Goody, 1976; McInnes & Curry, 1995; Zhang, 1999) and are less than one third of the average residence time for air parcels below 1,500 m in the Arctic (Stohl, 2006). This suggests that radiative cooling can drive Arctic stratocumulus formation during all seasons. In addition, a comparison of the distribution of the temperature at the time and height of saturation (Figure 2c) with the distribution of temperatures observed within Arctic stratocumulus clouds at Barrow (Figure 6l in Sedlar et al., 2012) indicates that these two distributions cover approximately the same temperature ranges. This suggests that many of the clear-sky profiles observed over Utqiaġvik could indeed produce stratocumulus layers in the Arctic through radiative cooling.

The radiative transfer calculations suggest that shortwave heating is unlikely to inhibit cloud formation by radiative cooling because solar zenith angles are too large in the Arctic. However, shortwave heating is still capable of delaying saturation: Shortwave heating offsets at least 25% of longwave cooling in 27% of profiles and at least 50% of longwave cooling in 11% of profiles (Figure 2e). Delays were largest in late spring, summer, and early autumn when average solar zenith angles are smallest at the NSA observatory. As a result, the median saturation time for stratocumulus-forming profiles is about 2 times longer in summer than in winter. However, it is important to note that air parcels below 1,500 m remain in the Arctic for more than twice as

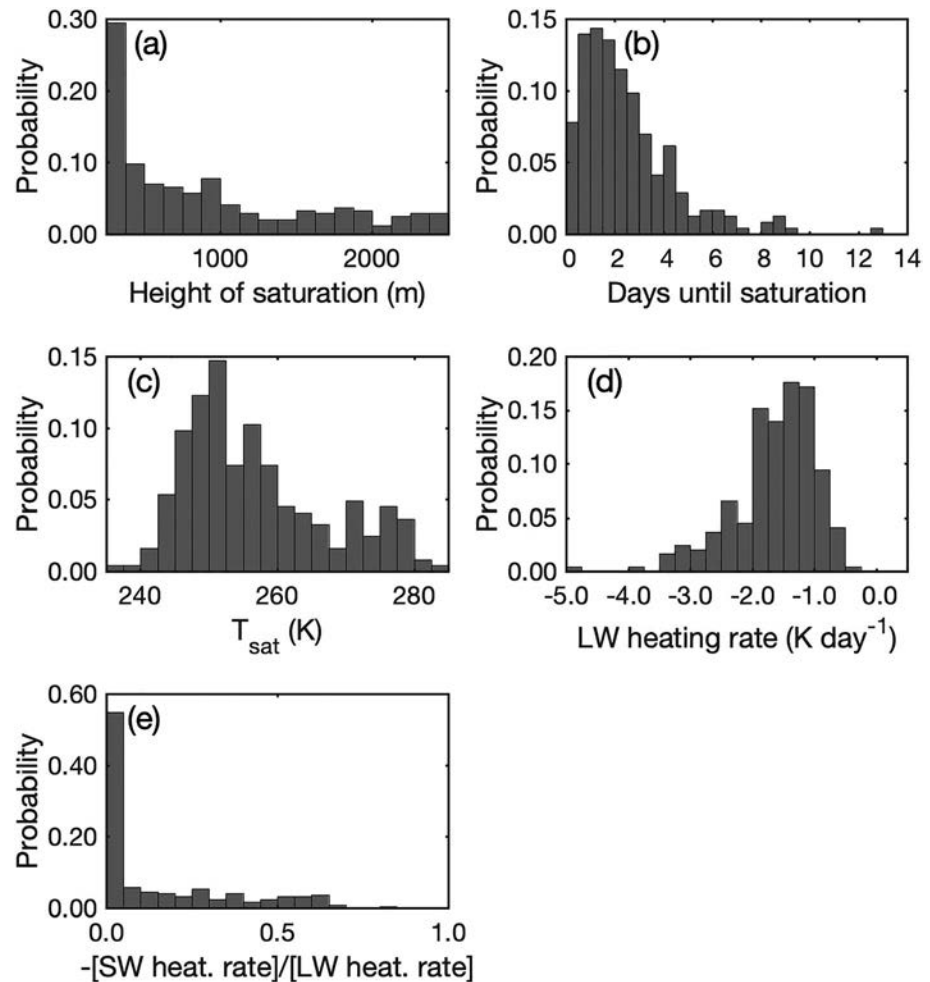


Figure 2. Probability distributions of (a) height at which each clear-sky profile saturates, (b) time required for each clear-sky profile to saturate when heated/cooled through only SW heating and LW cooling, and (c) the temperature at the time and height of saturation (T_{sat} , in Kelvin). Probability distributions of (d) the average LW heating rate and (e) the proportion of LW cooling that is offset by SW heating ($-\text{[SW heating rate]}/\text{[LW heating rate]}$) at the initial height of saturation. Only stratocumulus-forming profiles are included in these distributions. SW = shortwave; LW = longwave.

long in summer than in winter (Stohl, 2006). Therefore, the presence of solar radiation in summer does not necessarily make profiles less likely to saturate through radiative cooling.

The radiative transfer calculations on these static atmospheric profiles indicate that subsidence is much more effective than shortwave heating in inhibiting cloud formation. Figure 3 shows approximate percentages of stratocumulus-forming profiles that would saturate after 1, 2, and 5 days if mean vertical velocities from -5 to 5 mm/s were applied. Mean vertical velocities in this range are common across the Arctic (Klein et al., 2009; Morrison et al., 2011; Ovchinnikov et al., 2014; Stepanyuk et al., 2017). The times required for each stratocumulus-forming profile to saturate, with vertical motion, were estimated using the following procedure. First, the initial temperature, water vapor mixing ratio, and pressure at the height of saturation in each profile were recorded. Then, tendencies in those quantities associated with the given mean vertical velocity were calculated using thermodynamic principles. These tendencies, in addition to those associated with radiative cooling at that height, were then applied iteratively to the initial conditions until the temperature in the parcel fell to the dew point. The time required for this to occur served as the estimate of the time required for saturation to occur in the given profile, with the given vertical velocity. Figure 3 shows that the application of a mean vertical velocity of -1 mm/s would decrease the percentage of stratocumulus-forming profiles that saturate within 5 days, 2 days, and 1 day to 45%, 21%, and 11%, respectively. If a vertical velocity of -2 mm/s were imposed, the percentages would fall under 11%, and if a vertical velocity of -3 mm/s were

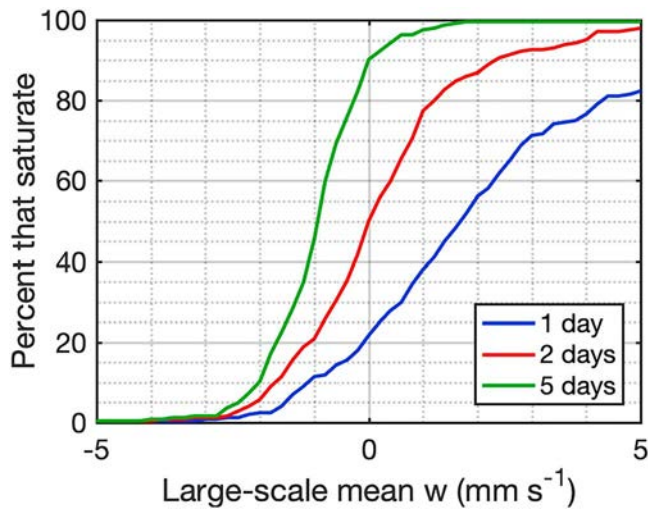


Figure 3. Percent of the 244 stratocumulus-forming profiles that saturate after 1 day (blue), 2 days (red), and 5 days (green) when a variety of large-scale mean vertical velocities (x axis) are imposed. Positive vertical velocities imply large-scale lift, while negative vertical velocities imply large-scale subsidence.

imposed, the percentages would all fall under 2%. While radiative cooling continues to promote cloud development even if large-scale subsidence is present, the low percentages imply that it is difficult for Arctic stratocumuli to form through clear-sky radiative cooling when subsidence velocity values exceed 4 mm/s.

Figure 3 shows that upward mean vertical velocities are very effective in accelerating saturation. If a mean vertical velocity of +1 mm/s were imposed, the proportion of stratocumulus-forming profiles that saturate within 1, 2, and 5 days would increase to 38%, 77%, and 98%, respectively. These percentages increase further when larger vertical velocities are imposed.

Inclusion of aerosols in the radiative transfer calculations would affect the results described above. Because moist atmospheric layers in the Arctic may originate from the midlatitudes (Devasthale et al., 2011), aerosols are likely to affect the cooling process. Dry aerosols in the Arctic are capable of both scattering and absorbing shortwave radiation but are small enough that their interaction with longwave radiation can be ignored (Curry, 1995). In the summer, these aerosols may slow cloud formation by enhancing clear-sky shortwave heating. However, estimates of dry aerosol contributions to heating rates are typically below 1 K/day (Shaw & Stamnes, 1980; Valero & Ackerman, 1985), so the presence of dry aerosols is unlikely to prevent cloud formation.

Wet aerosols or aerosols that have undergone deliquescence effectively absorb and scatter shortwave radiation and absorb and emit longwave radiation (Curry, 1995). In winter, these wet aerosols may accelerate cloud formation by enhancing longwave cooling rates. In summer, the overall effect of wet aerosols is less certain and depends on the aerosols' specific optical properties and the solar zenith angle. As noted above, the effects of aerosols are neglected here.

3. Cloud Formation Process

Radiative transfer calculations in the previous section showed that radiative cooling can lead to the formation of Arctic stratocumuli during all seasons. In this section, a SCM is used to approximate the process by which Arctic stratocumuli form in these elevated, stably stratified, moist layers after saturation occurs. The SCM is also used to test how the formation process is sensitive to the relative humidity (RH) above and below the layer of moisture with the forming cloud, the static stability of the layer of moisture, the solar zenith angle, and a number of other factors. A SCM is an appropriate tool for this task because it is capable of capturing feedbacks among radiative, turbulent, and cloud microphysical processes, which RRTM cannot capture. Simulations with the SCM are also computationally inexpensive, which allows a comprehensive examination of sensitivities using hundreds of simulations. This would not be feasible with large eddy simulations. Unfortunately, use of a SCM in place of large eddy simulations comes at an expense: The SCM does not resolve turbulent motions or horizontal variability, so the SCM's representations of entrainment, microphysical processes, and the behavior of cloud layers with low liquid water path (LWP) are incomplete. For this reason, the simulations in this section are not intended to provide a detailed description of the clouds' behavior in the real atmosphere. Rather, they are intended to provide a conceptual overview of the formation process and its sensitivities, which may be used to develop testable hypotheses and inform future studies using more sophisticated tools.

3.1. Model Description and Initialization

A full description of the SCM is available in Golaz (1997) so only a brief summary of the model is provided here. The SCM is based on the prediction of four prognostic variables: the horizontal wind velocity components (u and v), the ice-liquid potential temperature (θ_{il}), and the total water mixing ratio (r_t). These variables are predicted through four equations

$$\frac{\partial \bar{u}}{\partial t} = -\bar{w} \frac{\partial \bar{u}}{\partial z} + f(\bar{v} - v_g) - \frac{\partial}{\partial z} (\overline{w' u'}) \quad (1)$$

$$\frac{\partial \bar{v}}{\partial t} = -\bar{w} \frac{\partial \bar{v}}{\partial z} - f(\bar{u} - u_g) - \frac{\partial}{\partial z} (\overline{w' v'}) \quad (2)$$

$$\frac{\partial \bar{\theta}_{il}}{\partial t} = -\bar{w} \frac{\partial \bar{\theta}_{il}}{\partial z} - \frac{\partial}{\partial z} (\overline{w' \theta'_{il}}) + \left. \frac{\partial \bar{\theta}_{il}}{\partial t} \right|_{\text{rad}} + \left. \frac{\partial \bar{\theta}_{il}}{\partial t} \right|_{\text{sed}} \quad (3)$$

$$\frac{\partial \bar{r}_i}{\partial t} = -\bar{w} \frac{\partial \bar{r}_i}{\partial z} - \frac{\partial}{\partial z} (\overline{w' r'_i}) + \left. \frac{\partial \bar{r}_i}{\partial t} \right|_{\text{sed}} \quad (4)$$

where u_g and v_g represent the west-east and south-north components of the geostrophic wind velocity, w is the vertical velocity, the subscript “rad” indicates a tendency due to radiation, and the subscript “sed” represents a tendency due to sedimentation. Quantities with over bars signify Reynolds averaged quantities, while quantities with primes signify turbulent fluctuations.

Turbulence and turbulent fluxes are calculated following the 1.5-order turbulence closure scheme described in Bechtold et al. (1992) but with a few modifications. First, the eddy transfer coefficients for the momentum (K_m) and thermodynamic (K_h) variables are related through a ratio $\alpha = K_h/K_m$, where α is computed following Langland and Liou (1996). Second, the mixing and dissipation length scales are assumed to be equal and are computed as the square root of the product of two natural length scales. These natural length scales are computed as in Bechtold et al. (1992). Finally, the buoyancy flux is diagnosed from the vertical fluxes of θ_{il} and r_i if no condensate is present (Golaz, 1997, equation (2.97)) and from the vertical fluxes of θ_{il} , r_b , and the total ice mixing ratio r_i if condensate is present (Golaz, 1997, equation (2.105)).

The microphysical parameterization is based on the RAMS single-moment bulk microphysics scheme (Walko et al., 1995), which subdivides r_i into mixing ratios of water vapor, cloud water ($r_{\text{cl,d}}$), rain, pristine ice, snow, aggregates, graupel, and hail. The treatment of pristine ice and snow is replaced with a single particle property scheme. The dimensions, densities, growth rates, and fall speeds of pristine ice crystals are predicted using the bulk adaptive habit model, the details of which are described in Harrington et al. (2013) and Jensen et al. (2017). The adaptive habit model allows the aspect ratios of pristine ice crystals to evolve naturally and therefore allows a more realistic representation of depositional growth feedbacks. In addition, because some evidence suggests that heterogeneous ice formation requires the presence of liquid in the Arctic when temperatures are above -25°C (de Boer et al., 2011), the existing Meyers et al. (1992) ice nucleation scheme is replaced with a new scheme, based on those used by Morrison, Zuidema, et al. (2011), Solomon et al. (2014), and Ovchinnikov et al. (2014). The scheme only allows ice nucleation when $r_{\text{cl,d}} > 0.005$ g/kg and when the number concentration of ice crystals is below a specified threshold, N_{ice} . Because the scheme holds the ice number concentration approximately constant at N_{ice} within cloud layers, the scheme provides a simple means of varying the ice precipitation rate.

Irradiances are computed using a two-stream radiative transfer model, which is fully coupled to the model microphysics. A complete description of the radiative transfer code and optical properties can be found in Harrington (1997) and Harrington and Olsson (2001b), respectively. The surface is treated as a uniform slab with heat capacity set to $2.1 \times 10^4 \text{ J}\cdot\text{m}^{-2}\cdot\text{K}^{-1}$. The temperature of the slab responds to surface radiative, sensible heat, and latent heat fluxes with an e -folding timescale of 1.5 hr. Surface momentum fluxes are calculated using a surface roughness length of 1×10^{-4} m, a value that is typical for sea ice (Stull, 1988). The model predictive equations are discretized and integrated forward using a Crank-Nicolson type semiimplicit scheme.

All simulations are initialized with a consistent format, which includes several parameters that can be easily adjusted to test the formation process' sensitivity to a wide range of environmental characteristics. The general format for the initial thermodynamic profiles, which is based on composites from the 244 stratocumulus-forming profiles from section 2.2 (Figure S1 in the supporting information), is shown in Figure 4. The temperature profile contains a surface-based temperature inversion, which is likely to develop under clear-sky conditions. Between 600 and 1,400 m, the temperature lapse rate is set to a constant value γ . Above 1,400 m, the temperature decreases with height. The RH decreases from a peak of 100% at 1,000 m to

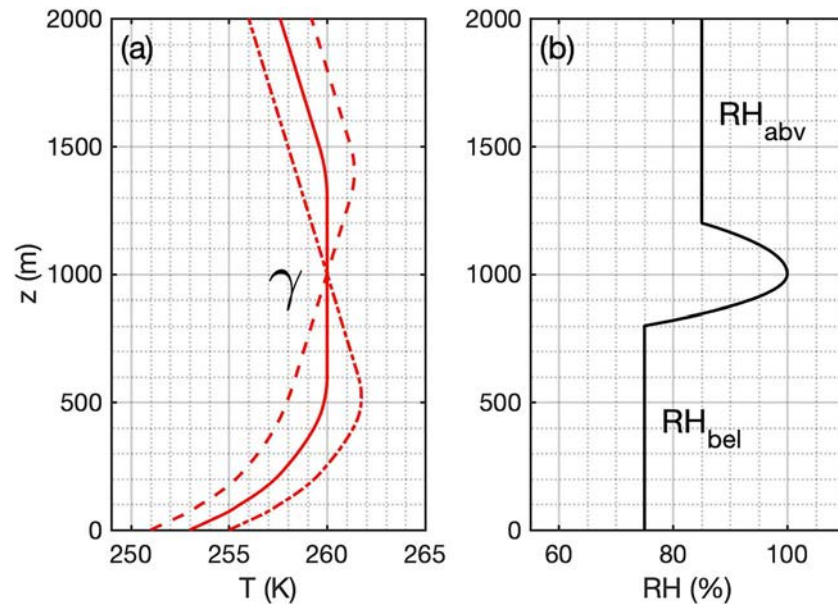


Figure 4. General format for the profiles of (a) temperature and (b) RH used to initialize all single column model simulations. The vertical temperature gradient between 600 and 1,300 m is labeled with “ γ .” The RH for $z \leq 800$ m is labeled with “ RH_{bel} ”, while the RH for $z \geq 1,200$ m is labeled with “ RH_{abv} ”. The initial profiles of temperature and RH for the *Baseline* (solid), *LessStable* (dot-dashed), and *MoreStable* (dashed) simulations are plotted. Only one RH profile is plotted because the initial profiles are identical in the three simulations. The *LessStable* and *MoreStable* simulations are introduced in section 3.3.3. RH = relative humidity.

specified values RH_{bel} at 800 m and RH_{abv} at 1,200 m. Below 800 m and above 1,200 m, the RH is uniform and equal to RH_{bel} and RH_{abv} , respectively. The initial water vapor profile is calculated from the initial temperature and RH profiles, and each simulation is initialized with a column-integrated LWP of 0.5 g/m^2 between 970 and 1,040 m. This is necessary for a cloud layer to form when subsidence, which is included to keep cloud layers at steady altitudes, is imposed. All simulations are initialized without ice condensate.

The maximum threshold number concentration of ice crystals (N_{ice}), number concentration of cloud droplets in cloudy grid cells (N_{cld}), and the solar zenith angle (SZA) are all held at constant values during each simulation. A background vertical velocity profile is imposed such that the mean vertical velocity is equal to w_{mean} above 1,000 m and varies linearly from 0 mm/s at the surface to w_{mean} at 1,000 m. The west-east and south-north components of the geostrophic wind are held at 3 m/s, and the initial wind components are set to their geostrophic values at all altitudes (3 m/s). Surface sensible and latent heat fluxes are specified as 0 W/m^2 because all simulated stratocumuli remain dynamically decoupled from the surface and do not directly interact with the surface fluxes. Both the effects of shortwave and longwave radiative heating are included in the simulations.

The formation of graupel, hail, and aggregates is turned off in all simulations. Although rain is permitted in all simulations, the model’s autoconversion parameterization (see Walko et al., 1995) does not permit rain to form for any values of N_{cld} and cloud water mixing ratio (r_{cld}) that occur in the SCM simulations.

Each simulation is run for a total of 10 hr. The domain extends from 0 to 2,000 m with the vertical grid spacing set to 10 m. The model time steps for the dynamical, microphysical, and thermodynamic calculations are 5 s, while the radiative fluxes are recalculated every 10 s.

A central assumption to these simulations is that the atmospheric columns in which the cloud layers form remain intact as they drift across the Arctic. Under this assumption, prescription of θ_{11} and r_t tendencies to represent the thermodynamic effects of horizontal advective processes are unnecessary. Investigating how Arctic stratocumuli respond to advective tendencies is beyond the scope of this study but would be a fruitful subject for future research.

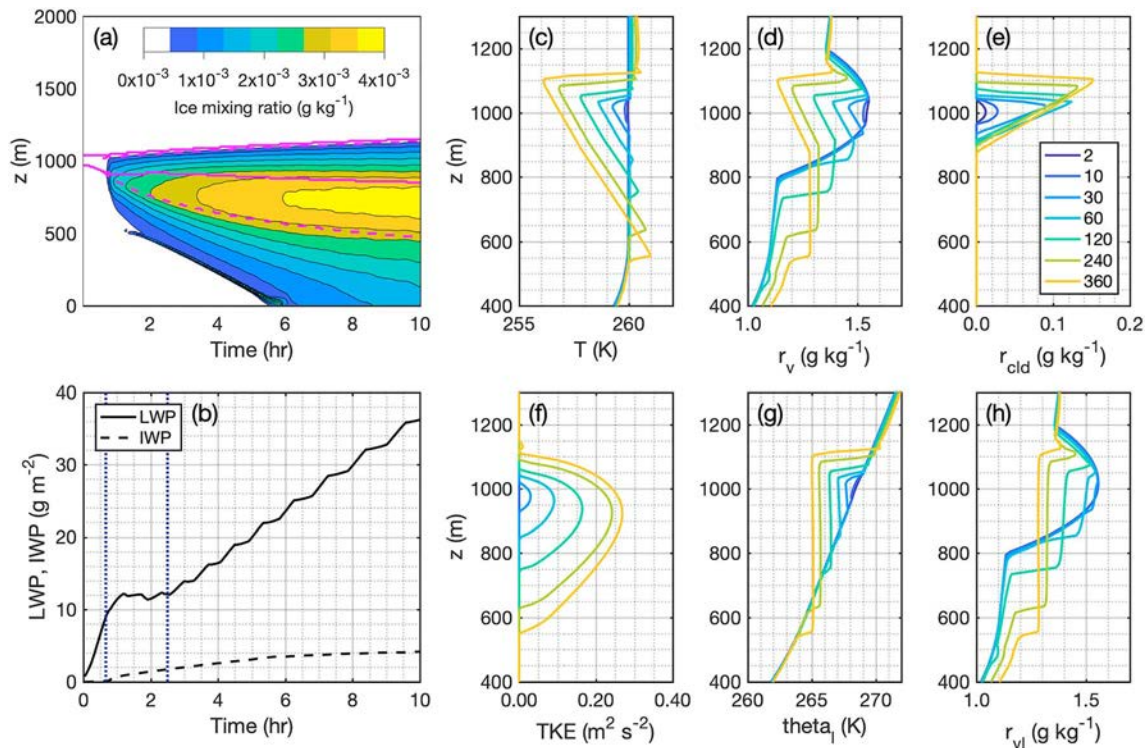


Figure 5. For the *Baseline* simulation: (a) time series of cloud boundaries (solid magenta), mixed-layer boundaries (dashed magenta), and profiles of ice mixing ratio (g/kg^{-1} ; contoured). (b) Time series of simulated LWP and ice water path (IWP). The two vertical dotted lines mark the approximate divisions between the three stages of the formation process. Plotted profiles of (c) temperature, (d) water vapor mixing ratio, (e) cloud water mixing ratio, (f) turbulent kinetic energy, (g) liquid potential temperature, and (h) vapor-plus-liquid mixing ratio at 2, 10, 30, 60, 120, 240, and 360 min after the beginning of the *Baseline* simulation. The colors corresponding to each time plotted in (c)–(h) are shown in the legend in (e). LWP = liquid water path.

3.2. Baseline Simulation

A single *Baseline* simulation is used to outline the process by which Arctic mixed-phase stratocumulus cloud layers form by clear-sky radiative cooling in the SCM. The *Baseline* simulation is initialized with $RH_{\text{abv}} = 85\%$, $RH_{\text{bel}} = 75\%$, $\gamma = 0 \text{ K}/\text{km}$, $N_{\text{ice}} = 1 \text{ L}^{-1}$, $N_{\text{cld}} = 100 \text{ cm}^{-3}$, $SZA = 90^\circ$, and $w_{\text{mean}} = -3.6 \text{ mm}/\text{s}$ and begins with $0.5 \text{ g}/\text{m}^2$ of cloud water distributed between altitudes 970 and 1,040 m.

The stratocumulus layer in the *Baseline* simulation forms in three stages. In the first stage, the cloud layer grows rapidly through a feedback between radiative cooling and condensation. As radiative cooling promotes condensation within the cloud layer (Figures 5d and 5e), the layer's emissivity increases and radiative cooling intensifies. This, in turn, increases the condensation rate in a positive feedback loop. Such a feedback is also visible in simulations by Garrett et al. (2009) and Zhang (1999). Because of the feedback, the layer's LWP rises to $11.4 \text{ g}/\text{m}^2$ by the end of simulation hour 1 (Figure 5b). Ice production is weak during this first stage, and the small amount of ice that forms falls out of the cloud layer and sublimates in the region below.

Cloud top temperature and r_v inversions form naturally during the first stage and strengthen through the remainder of the simulation (Figures 5c and 5d). These inversions form because cooling and condensation occur more quickly within the cloud layer than above the cloud top. Cloud water is continuously present within the inversion because the turbulent and radiative tendencies in r_t and θ_{il} are such that the sum of r_v and r_{cld} is always greater than the saturation vapor mixing ratio with respect to liquid within the inversion. When this occurs, the model diagnoses that cloud water is present in the inversion by default.

By the simulation's 30th min, thermal destabilization by radiative cooling leads to the development of turbulence within the cloud layer. Over the following 10 min, the turbulence intensifies and an elevated, cloud-driven mixed-layer forms (Figures 5a and 5f), as in simulations by McInnes and Curry (1995) and Zhang (1999). In this study, a cloud-driven mixed layer is defined as a region in which the turbulent kinetic energy exceeds $0.02 \text{ m}^2/\text{s}^2$ and the ice-liquid potential temperature (θ_{il}) deviates by less than 0.1 K from the

value of θ_{il} in the center of the cloud layer. The 0.1 K threshold is arbitrary but is effective in identifying cloud-driven mixed layers from the SCM output.

Once the mixed layer forms, the second stage of the formation process begins. The second stage is characterized by a rapid expansion of the cloud-driven mixed layer through entrainment: between simulation hours 1 and 2, the average entrainment rates at the mixed-layer base and top are 26.3 and 9.0 mm/s, respectively. Rapid entrainment modifies the thermodynamic properties of the mixed layer and allows the mixed layer to extend well below the cloud base (Figure 5a). The second stage is also characterized by an intensification of ice precipitation, which occurs because turbulence keeps individual ice crystals in ice supersaturated environments for longer, permitting them to grow larger through deposition before falling out of the mixed layer.

The evolution of the cloud layer's first-order properties during the second stage can be understood through the evolution of the mixed layer's properties. The cloud top remains approximately 30 m above the mixed-layer top and rises with the mixed-layer top. The cloud layer's LWP changes approximately with the cloud thickness because the cloud layer's profile of r_{clid} is nearly moist adiabatic. The cloud base changes with the mixed layer's lifting condensation level, which is determined by profiles of liquid potential temperature (θ_l) and vapor-plus-liquid mixing ratio ($r_{vl} = r_v + r_l$) in the mixed layer. These profiles grow increasingly uniform with time (Figures 5g and 5h) and shift according to the mixed layer's budgets of θ_l and r_{vl} , which may be written in terms of the mixed-layer mean θ_l and r_{vl} (θ_{lM} and r_{vlM} , respectively)

$$\frac{d\theta_{lM}}{dt} = \frac{1}{\int_{z_b}^{z_t} \bar{\rho} dz} \int_{z_b}^{z_t} \left[-\bar{\rho} \bar{w} \frac{\partial \bar{\theta}_l}{\partial z} - \bar{\rho} \frac{\partial}{\partial z} (\overline{w' \theta'_l}) - \frac{1}{c_p} \left(\frac{p_0}{\bar{p}} \right)^{\frac{R}{c_p}} \frac{\partial \overline{F_{\text{net}}}}{\partial z} + \bar{\rho} \frac{L_s}{c_p} \left(\frac{p_0}{\bar{p}} \right)^{\frac{R}{c_p}} \frac{d\bar{r}_i}{dt} \Big|_{d,s,f,m} \right] dz \quad (5)$$

and

$$\frac{dr_{vlM}}{dt} = \frac{1}{\int_{z_b}^{z_t} \bar{\rho} dz} \int_{z_b}^{z_t} \left[-\bar{\rho} \bar{w} \frac{\partial \bar{r}_{vl}}{\partial z} - \bar{\rho} \frac{\partial}{\partial z} (\overline{w' r'_{vl}}) - \bar{\rho} \frac{d\bar{r}_i}{dt} \Big|_{d,s,f,m} \right] dz \quad (6)$$

where z_t is the height of the mixed-layer top, z_b is the height of the mixed-layer base, ρ is the density of air, p is the atmospheric pressure, F_{net} is the net radiative flux, c_p is the specific heat of dry air at constant pressure, p_0 is the reference pressure (1,000 hPa) used to calculate θ_l , R is the dry air gas constant, and L_s is the enthalpy of sublimation of water. $\overline{w' \theta'_l}$ and $\overline{w' r'_{vl}}$ denote the vertical turbulent fluxes of θ_l and r_{vl} , respectively, while $\frac{d\bar{r}_i}{dt} \Big|_{d,s,f,m}$ represents the tendency in the average ice mixing ratio due to deposition, sublimation, freezing, and melting. When multiplied by the coefficient outside the integral, the four added terms on the right-hand side of equation (5) represent (from left to right) the tendencies in θ_{lM} due to the mean vertical velocity, turbulent flux convergence, radiative flux convergence, and the formation/destruction of ice. Similarly, the three added terms on the right-hand side of equation (6) represent the tendencies in r_{vlM} due to the mean vertical velocity, the turbulent flux convergence, and the formation/destruction of ice. Because variations in $\bar{\rho}$ are small over the depth of the cloud-driven mixed layer, the turbulent flux convergence terms approximate the changes in θ_{lM} and r_{vlM} due to the entrainment of air at both mixed-layer boundaries. Time series of each budget term are plotted in Figure 6. Note that the budget terms are only plotted after the simulation's 40th min because a region of uniform θ_{il} (required for the classification of the mixed layer) only develops at that time.

The cloud LWP is approximately constant during a majority of the second stage of the formation process (Figure 5b) because a balance occurs among the effects of entrainment, radiative cooling, and ice precipitation. Entrainment at the cloud top produces a positive tendency in the LWP: As the cloud top rises through entrainment, circulations become deeper and the cloud layer's adiabatic LWP increases. Longwave emission by the cloud also produces a positive tendency in the LWP by cooling the mixed layer. This tendency is large at first but weakens as the mixed layer expands and attains a larger total heat capacity (Figure 6). Tendencies associated with entrainment from below and ice growth oppose the tendencies due to the rising cloud top and longwave emission. The entrainment of air from below produces a negative LWP tendency by drying

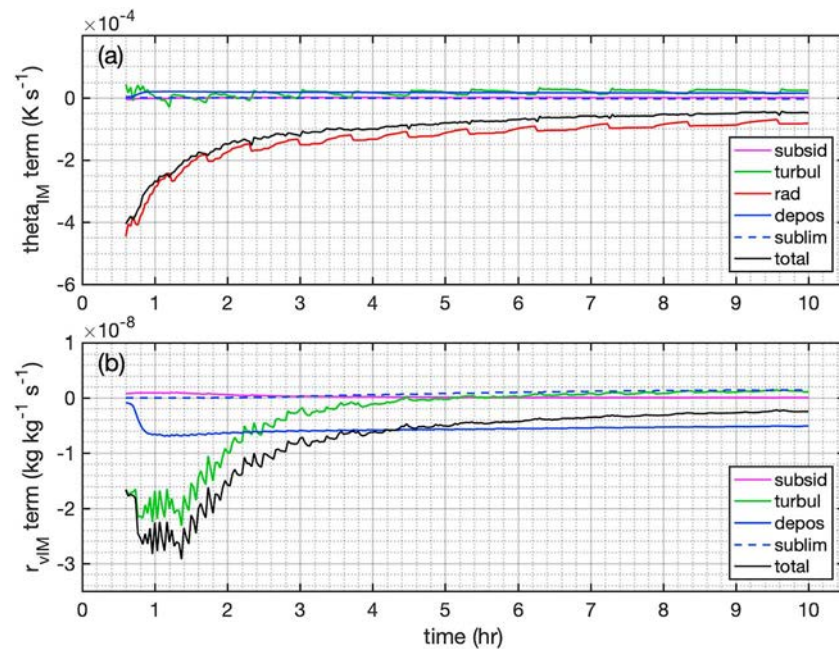


Figure 6. Time series of each budget term for (a) θ_{IM} and (b) r_{vIM} over the entire 10 hr of the *Baseline* simulation. The magenta lines show time series of the subsidence term, the green lines of the turbulent term, the red line of the radiation term, and the blue lines of the ice formation/destruction term. The ice formation/destruction term is split into two: The solid blue lines show the effect of ice formation through deposition, while the dashed blue lines show the effect of ice destruction through sublimation. Neither freezing nor melting occurs during the simulation.

the mixed layer. This tendency is extreme early in the second stage but moderates as the mixed layer expands and entrainment at the mixed-layer base slows (Figure 6). The depositional growth of ice precipitation also produces a negative LWP tendency by consuming vapor and causing latent heating (Figure 6). For much of the second stage of the formation process, all of these tendencies balance almost perfectly, allowing the LWP to remain nearly constant.

By simulation hour 2.5, entrainment rates slow and the cloud layer in the *Baseline* simulation gradually transitions to the third stage of its formation process. During the third stage, the mixed layer remains well mixed, so that the cloud layer's base, top, and LWP are still determined by the mixed layer's properties. However, the balance that governs the mixed layer's properties shifts (Figure 6). For example, the rate at which entrainment from below dries the mixed layer slows because entrainment at the mixed-layer base slows (Figure 5a) and because the region below the mixed-layer base moistens through the sublimation of ice precipitation (Figure 5d). In addition, ice precipitation begins sublimating within the lower portion of the mixed layer because that region becomes subsaturated with respect to ice, which cools and returns vapor to the mixed layer (Figure 6). Overall, the cloud layer's LWP increases consistently because the effects of radiative cooling and the rising cloud top outweigh the effect of depositional ice growth (Figure 5b). After simulation hour 10, the cloud layer's LWP reaches 36.1 g/m^2 .

3.3. Sensitivity Tests

Changes in RH_{abv} , RH_{bel} , SZA , γ , N_{ice} , N_{cl} , and w_{mean} affect the formation process by modifying the effects of radiation, entrainment, and ice processes on the mixed layer's properties. In this subsection, the formation process' sensitivities to these factors are explored using several large sets of simulations. A set of 289 simulations (*SensMoisture*), in which RH_{abv} and RH_{bel} are both varied from 15% to 95% by intervals of 5% (such that a single simulation is run for each combination of RH_{abv} and RH_{bel}), is used to examine sensitivities to RH_{abv} and RH_{bel} . Another two sets, which are both identical to *SensMoisture* except in that the SZA is set to 80° in one (*SensSZA80*) and 70° in the other (*SensSZA70*), are used to test the sensitivity to the SZA . Sensitivities to γ are investigated with two additional sets of 289 simulations, which are both identical to *SensMoisture* except in that γ is set to -4 K/km in one (*SensLoStability*) and $+4 \text{ K/km}$ in the other (*SensHiStability*).

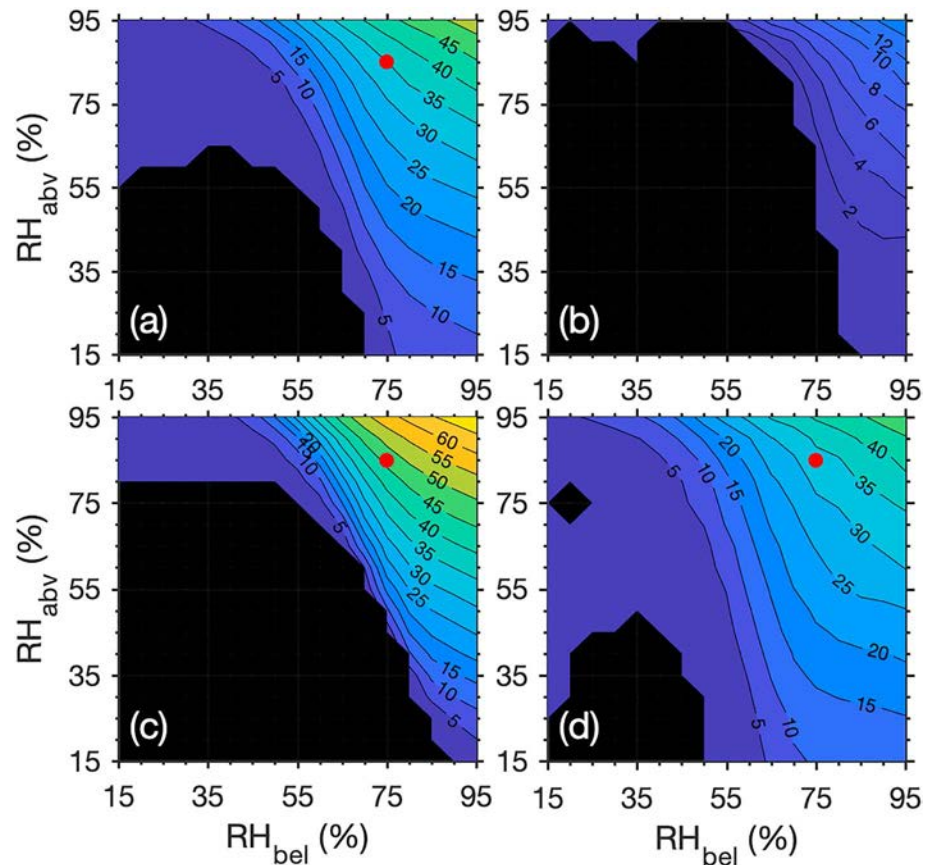


Figure 7. The average liquid water paths (g/m^2) between simulation hours 9 and 10 contoured as a function of the RH_{abv} and RH_{bel} used to initialize the simulation for all simulations in (a) the *SensMoisture* set, (b) the *SensSZA80* set, (c) the *SensLoStability* set, and (d) the *SensHiStability* set. Combinations of RH_{abv} and RH_{bel} that yield clouds that dissipate before simulation hour nine are shaded in black. The red dots in (a), (c), and (d) represent the liquid water paths for the *Baseline*, *LessStable*, and *MoreStable* simulations, respectively. RH = relative humidity.

The profile composites used to inform the design of these sets are shown in Figure S1. The LWPs of the cloud layers, averaged over the final simulation hour, for all of the simulations in the *SensMoisture*, *SensSZA80*, *SensLoStability*, and *SensHiStability* sets are contoured as a function of RH_{abv} and RH_{bel} in Figure 7. Note that no LWPs are plotted for simulations in the *SensSZA70* set because all cloud layers in that set dissipate before simulation hour 9. Sensitivities of the formation process to N_{ice} , N_{cld} , and w_{mean} are also investigated using similar sets of 289 simulations, but contour plots of LWPs for these simulations are not shown. Although most cloud layers in these simulations form in the same three stages as in the *Baseline* simulation, the cloud layers in some simulations dissipate before the third stage begins.

3.3.1. Sensitivity to $RH_{\text{abv}}/RH_{\text{bel}}$

The *SensMoisture* set shows that the formation process' sensitivity to the initial RH_{bel} and RH_{abv} is dependent on the initial values of those two parameters. Simulations initialized with $RH_{\text{bel}} < 85\%$ are more sensitive to RH_{bel} than RH_{abv} (Figure 7a) because simulation-averaged entrainment rates are larger at the mixed-layer base (11 mm/s) than at the mixed-layer top (3 mm/s), allowing the air below to have a greater influence on the mixed layer's thermodynamic properties. Meanwhile, simulations initialized with $RH_{\text{bel}} \geq 85\%$ are more sensitive to RH_{abv} (Figure 7a) because ice precipitation from the cloud grows through vapor deposition below the mixed-layer base, where conditions are supersaturated with respect to ice. The depositional growth forces the RH with respect to ice below the mixed-layer base toward 100% as each simulation progresses, homogenizing the thermodynamic conditions in that region, and reducing the formation process' sensitivity to the initial RH_{bel} . A similar homogenization occurs when $RH_{\text{bel}} < 85\%$ as ice precipitation sublimates in the region below the mixed-layer base but occurs more slowly and is unable to outweigh the effect of the differing entrainment rates.

Interestingly, many simulations that are moist above ($RH_{\text{abv}} \geq 65\%$) and dry below ($RH_{\text{bel}} < 65\%$) do not dissipate due to the rapid influx of dry air from below (Figure 7a). At the beginning of the second stage of the formation process, the LWP of each of these layers declines rapidly in response to an influx of dry air from below (Figure S2b). As the LWP decreases, turbulence within the mixed layer weakens because buoyant production of turbulence slows (Figure S2d). The weakening turbulence prevents the mixed layer from entraining further dry air from below and causes the effects of radiative cooling, ice formation, and entrainment on the cloud's LWP to balance. Consequently, the LWPs of these layers steady at values below 2 g/m^2 , on average (Figure S2b). By the simulation hour 4, the LWP once again begins to rise in most of these simulations (Figure S2b). However, the rise in LWP occurs very slowly because the LWP is limited by the presence of dry air below. As each cloud's LWP and emissivity rise, turbulence within the mixed layer intensifies and the entrainment of dry air from below resumes. As a result of this limitation, the LWP remains under 5 g/m^2 in most simulations (Figure 7a). It is important to note that the SCM's representation of this low-LWP quasi steady state is incomplete because the model is unable to resolve horizontal heterogeneities, which would likely develop in cloud layers with such small LWPs.

Simulations that are dry both above and below dissipate by cloud thinning before the end of the simulation (Figure 7a). In these simulations, drying through entrainment at both mixed-layer boundaries and warming/drying through ice growth are sufficient to desiccate all liquid within the cloud layer. Cloud top entrainment instability does not drive the dissipation of any cloud layer in the SensMoisture, SensLoStability, SensHiStability, or SensSZA80 sets because the vapor jump at the mixed-layer top is always too small to support buoyancy reversal, according to the Randall-Deardorff criterion (Deardorff, 1980; Randall, 1980).

Overall, the sensitivities to RH_{abv} and RH_{bel} in the SensMoisture set are qualitatively similar to those shown in large eddy simulations by Solomon et al. (2014). However, the sensitivities are more severe because entrainment, especially at the mixed-layer base, is more rapid during the formation process than later in an Arctic stratocumulus cloud's lifetime.

3.3.2. Sensitivity to SZA

The SensSZA80 and SensSZA70 sets show that the addition of solar radiation results in several changes in the formation process. First, the mixed layer cools more slowly because solar absorption offsets a portion of the longwave emission. Second, the rate at which the cloud top rises through entrainment slows because the buoyant production of turbulence near the cloud top is less intense. Third, entrainment at the mixed-layer base slows because turbulence is weaker; this causes the mixed layer to dry more slowly when the atmosphere below is dry. Finally, ice precipitation is less intense because the cloud layer is shallower. Overall, the first and second effects outweigh the third and fourth effects. Consequently, when the SZA is set to 80° , a greater number of clouds dissipate, and clouds that do not dissipate attain much smaller LWPs than in corresponding simulations without solar radiation (Figure 7b). These effects are even more pronounced when the SZA is decreased to 70° : While cloud layers do form in these simulations, they all dissipate before simulation hour 9.

3.3.3. Sensitivity to γ

The general sensitivities to γ (shown in Figures 7c and 7d) are most clearly understood through a close examination of two additional simulations that are similar to the Baseline simulation. One is initialized with $RH_{\text{abv}} = 85\%$, $RH_{\text{bel}} = 75\%$, and $\gamma = -4 \text{ K/km}$ (the *LessStable* simulation) and the other initialized with $RH_{\text{abv}} = 85\%$, $RH_{\text{bel}} = 75\%$, and $\gamma = +4 \text{ K/km}$ (the *MoreStable* simulation). The T and RH profiles used to initialize these two simulations are plotted in Figure 4.

Over the first 2.5 hr of the *LessStable* simulation, the LWP rises more slowly than in the Baseline simulation (Figure 8b) for several reasons. First, the cloud-driven mixed layer forms earlier in the *LessStable* simulation, which prevents the LWP from growing as large before the entrainment of dry air from below begins (Figure 8c). Second, entrainment occurs more rapidly in the *LessStable* simulation after the mixed layer forms because weaker virtual potential temperature inversions form at both mixed-layer boundaries (Figure 8a). This rapid entrainment dries the mixed layer more rapidly than in the Baseline simulation (Figure 8d), slows the rate at which the mixed layer cools through longwave emission (Figure 8c), and therefore suppresses the growth of liquid. During the remainder of the *LessStable* simulation, the LWP rises more rapidly than in Baseline because the cloud top rises more rapidly (Figure 8a), and a greater fraction of ice

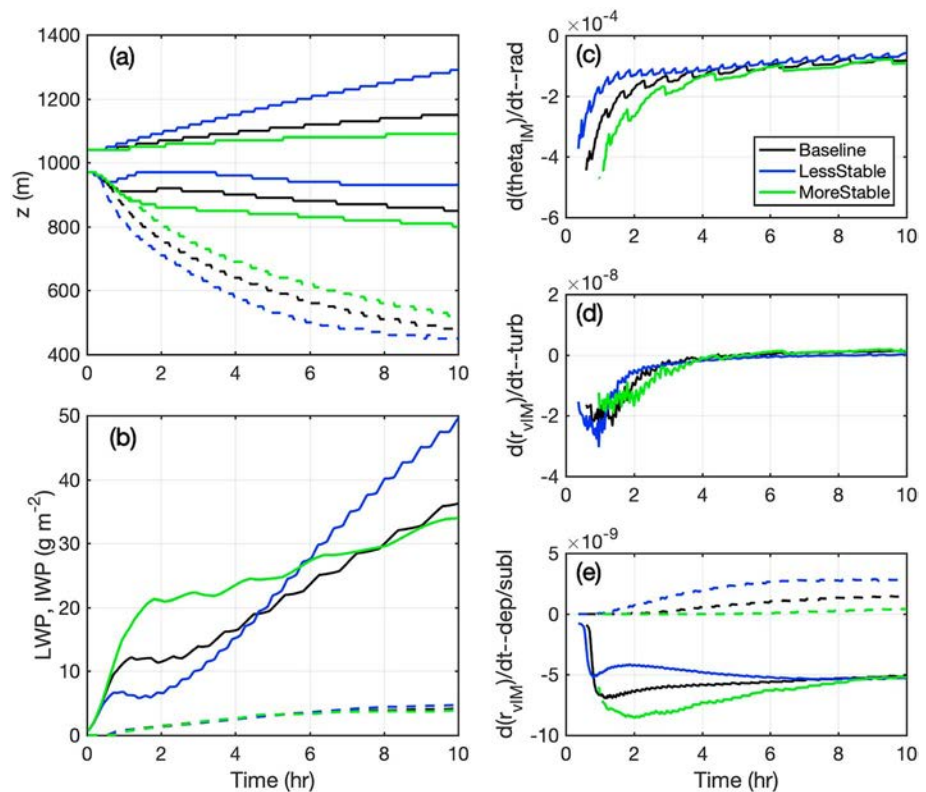


Figure 8. Time series for the *Baseline* (black lines), *LessStable* (blue lines), and *MoreStable* (green lines) simulations of (a) the cloud boundaries (solid lines) and mixed-layer base (dashed lines), (b) LWP (solid lines) and IWP (dashed lines), (c) radiation term of the mixed layer θ_{IM} budget (K/s), (d) turbulent flux convergence term of the mixed layer r_{vIM} budget ($kg \cdot kg^{-1} \cdot s^{-1}$), and (e) ice formation (solid lines) and destruction (dashed lines) terms of the mixed layer r_{vIM} budget ($kg \cdot kg^{-1} \cdot s^{-1}$). LWP = liquid water path; IWP = ice water path.

precipitation sublimates in the cloud-driven mixed layer, which extends further below cloud base (Figures 8a and 8e). By simulation hour 10, the LWP in *LessStable* is larger than in *Baseline* (Figure 8b).

A comparison of the *MoreStable* and *Baseline* simulations shows that increasing the static stability has the opposite effect. During the first 2.5 hr of *MoreStable*, the LWP rises more quickly than in *Baseline* because the mixed layer forms later and entrainment occurs more slowly (Figures 8a, 8b, and 8d). Later, the LWP rises more slowly in *MoreStable* because entrainment at cloud top occurs more slowly and because a smaller fraction of ice precipitation sublimates in the subcloud mixed layer (Figures 8a and 8e).

The differences among the *LessStable*, *MoreStable*, and *Baseline* simulations help explain the sensitivities revealed in the *SensLoStability* and *SensHiStability* sets (Figures 7c and 7d). In general, cloud layers that form under lower static stability entrain more rapidly at both mixed-layer boundaries. If dry air is present above or below, dry air is incorporated into the mixed layer more rapidly, especially during the second stage of the formation process. This increases the likelihood that cloud layers will dissipate or attain low LWPs. If no dry air is present, the more rapid entrainment at cloud top allows the cloud layers to attain larger LWPs because the cloud top rises more rapidly. Conversely, if the static stability is larger, entrainment occurs more slowly at both mixed-layer boundaries, which makes cloud layers that form in dry environments less likely to dissipate but prevents cloud layers that form in moist environments from attaining such large LWPs.

3.3.4. Sensitivity to N_{ice} , N_{cld} , and w_{mean}

When N_{ice} is set to $0 L^{-1}$ so that no ice precipitation forms, all cloud layers attain larger LWPs because their mixed layers no longer warm and dry through ice growth. Cloud layers also become more sensitive to the initial RH_{bel} because ice precipitation no longer homogenizes the thermodynamic conditions below the mixed-layer base. Meanwhile, when N_{ice} is set to $3 L^{-1}$ so that ice precipitation is heavier, cloud layers in all but the moistest environments dissipate before simulation hour 10. Layers that do persist through the

end of the simulation attain LWPs under 15g/m^2 . These sensitivities are broadly consistent with those revealed by large eddy simulations by Harrington and Olsson (2001a), Morrison, de Boer, et al. (2011), and Ovchinnikov et al. (2011).

When N_{cld} is set to 400 cm^{-3} instead of 100 cm^{-3} , the cloud layers grow more rapidly during the first stage of the formation process. This is because cloud emissivity increases more quickly with cloud LWP, so that the feedback between radiative cooling and condensation that drives liquid growth occurs more quickly. This is consistent with findings by Garrett et al. (2009). In addition, there is more entrainment at cloud top during the second and third stages of the formation process, which makes the cloud layers more sensitive to the initial RH_{abv} than in simulations with N_{cld} equal to 100 cm^{-3} . When N_{cld} is set to 20 cm^{-3} , the direct opposite occurs.

When w_{mean} is set to 0 instead of -3.6 mm/s , cloud layers attain larger LWPs and are less likely to dissipate because the cloud top rises more rapidly. This sensitivity becomes even more pronounced when w_{mean} is further increased to 2 mm/s . In contrast with findings by Young et al. (2018), subsidence in the SCM does not drive a feedback between entrainment and in-cloud convection that allows Arctic stratocumuli to attain larger LWPs. The absence of this feedback is likely due to the SCM's less detailed treatment of turbulence and entrainment.

4. Discussion

Arctic stratocumulus clouds form in stable atmospheric layers when those layers cool to saturation through a mixture of radiative cooling, synoptic/mesoscale forcing (lifting), and mixing. The radiative transfer calculations in section 2 demonstrate that radiative cooling is capable of driving Arctic stratocumulus formation at Utqiagvik without assistance from other processes. This is because radiative cooling is able to cool profiles to saturation over timescales that are less than one third the average residence time for air parcels in the Arctic (Figure 2b). However, the calculations also show that subsidence is very effective in inhibiting cloud formation by radiative cooling: When subsidence velocities of 4 mm/s are imposed, only 23% of the stratocumulus-forming profiles analyzed in section 2 saturate within 5 days.

To determine if these findings generalize over the Arctic pack ice, we have compared radiosonde observations from the NSA observatory (from 1 January 2012 to 31 December 2015) with observations from the year-long, 1997–1998 Surface Heat Budget of the Arctic (SHEBA) expedition (Moritz, 2017). To isolate cloud-free launches at both locations, we eliminated all launches that observed dew point depressions of less than 1 K at any altitude and all launches that did not rise above 13,000 m. We then calculated the minimum dew point depression between 250 and 2,500 m for the remaining profiles and plotted distributions of these values in Figure 9. According to Figure 9, dew point depressions below 4 K were observed below 2,500 m in a majority of clear-sky profiles at both locations, both overall and in winter. This implies that dew point depressions less than 4 K are commonly observed in the lower Arctic atmosphere and are not necessarily associated with strong advection events. Assuming an average radiative cooling rate of 1.5 K/day (common at Utqiagvik; see Figure 2d) and assuming no mean vertical motion, a majority of profiles at both locations would have saturated within 2.67 days of the time at which they were observed. This is consistent with results in Figure 2b and suggests that radiative cooling is also capable of driving Arctic stratocumulus formation over the pack ice. Unfortunately, the radiative transfer calculations do not indicate whether radiative cooling, synoptic/mesoscale forcing, or mixing is the primary driver of cloud formation at Utqiagvik or over the pack ice; estimating these relative contributions to cloud formation could be a very productive avenue for future research.

The SCM's representation of formation by radiative cooling in stable atmospheric layers is conceptually consistent with the existing literature. In the first stage of the formation process, a feedback between radiative cooling and condensation drives a rapid growth of liquid. This feedback was also observed in SCM and large eddy simulations by Zhang (1999) and Garrett et al. (2009), which examined how liquid-only Arctic stratocumuli form by radiative cooling. Shortly thereafter, a cloud-driven mixed layer forms due to thermal destabilization by radiative cooling (as in McInnes & Curry, 1995; Zhang, 1999; Garrett et al., 2009), marking the beginning of the second stage of the formation process. In the second stage, a balance between the effects of radiative cooling, entrainment, and ice precipitation determines the cloud layer's evolution. Entrainment is

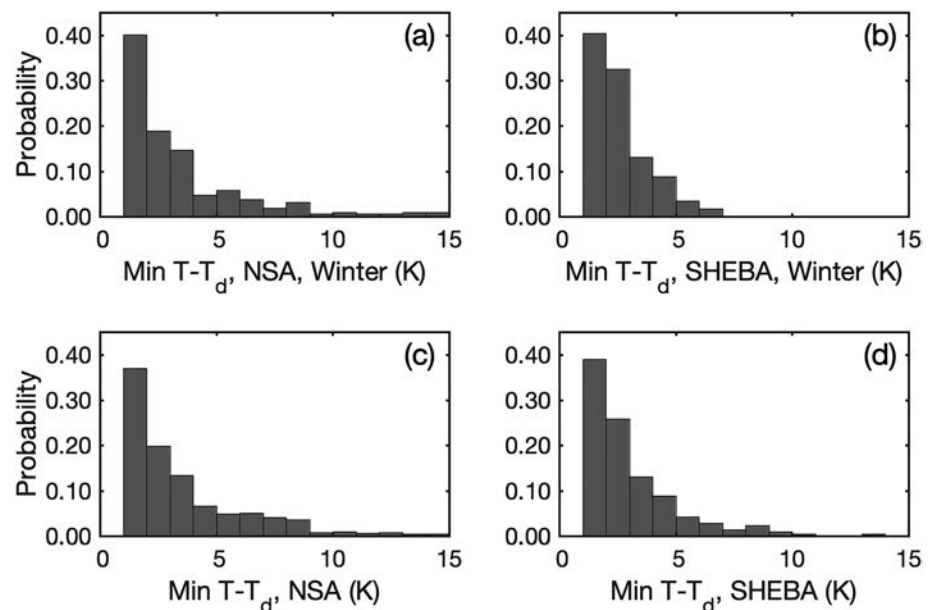


Figure 9. Distributions of the minimum dew point depression between 250 and 2,500 m in all cloud-free soundings launched from the NSA observatory (years 2012–2015) and from SHEBA. (a, b) Soundings launched only in winter. (c, d) Soundings launched during all seasons. NSA = North Slope of Alaska; SHEBA = Surface Heat Budget of the Arctic.

particularly important during this stage because it is so rapid, especially at the mixed-layer base. The cloud layer then transitions to the third stage of its formation process as entrainment at the mixed-layer base slows. In the third stage, the cloud layer still evolves through a balance between these three processes, but entrainment plays a much weaker role in that balance.

The Baseline simulation and large eddy simulations by Sulia et al. (2014) present a similar picture of why Arctic stratocumuli persist for long periods of time, despite their colloidal instability: In these simulations, warming and drying through the depositional growth of ice is too weak to outweigh liquid generation by radiative cooling and the rising cloud top. The simulations in the SensMoisture, SensLoStability, SensHiStability, and SensSZA80 sets also suggest that wintertime Arctic stratocumuli may persist for long periods of time because temperatures are too cold to support cloud top entrainment instability. For a mean inversion temperature of 258 K, mean inversion pressure of 925 hPa, maximum r_{clid} of 0.1 g/kg, and temperature inversion strength of 3 K, a vapor jump of at least -1.6 g/kg is necessary to support buoyancy reversal, according to the Randall-Deardorff criterion. This vapor jump could never be observed because it is greater than the saturation vapor mixing ratio at 258 K, which is about 1.3 g/kg. At warmer wintertime temperatures and with weaker temperature inversions, buoyancy reversal is possible but still unlikely given the severity of the variations in vapor mixing ratio that are required for buoyancy reversal to occur.

The Baseline SCM simulation indicates that ice precipitation plays a complex role in the formation process. The primary effect of ice precipitation is to warm and dry the mixed layer through latent heating and the consumption of water vapor during depositional growth. However, a portion of the primary effect is offset when ice precipitation sublimates in the lower portion of the cloud-driven mixed layer. This occurs when the mixed layer mixes vigorously and extends far enough below the cloud base for the lower portion of the mixed layer to become subsaturated with respect to ice. Both effects have been noted in large eddy simulations of mature Arctic stratocumuli (Morrison, Zuidema, et al., 2011; Solomon et al., 2014; Solomon et al., 2015; Sulia et al., 2014). A secondary effect occurs when ice precipitation sublimates or grows by deposition in the region below the mixed-layer base. If the region below is dry, ice precipitation moistens and cools air that is later entrained, and if the region below is moist, ice precipitation warms and dries air that is later entrained. Sensitivity tests show that this modification reduces the sensitivity of the formation process to the initial RH_{bel} . In addition, it is possible that sublimation/deposition below the mixed-layer base affects the entrainment rate at the mixed-layer base by strengthening or weakening the inversion there; however, this effect was difficult to isolate in the SCM simulations.

In the Baseline simulation, the stratocumulus layer does not interact with surface fluxes because the surface fluxes are set to 0 W/m^2 . If nonzero surface fluxes had been specified, interactions would still have been minimal because a 7 K surface-based temperature inversion separates the cloud layer and surface, making turbulent coupling between the surface and cloud layer unlikely. However, interactions with turbulent fluxes are likely to be important under different circumstances, such as when clouds form closer to the surface (Figure 2a) or when surface-based temperature inversions are weaker. These interactions would most likely be similar to interactions that occur between stratocumuli and surface fluxes in the subtropics and midlatitudes (summarized in Wood, 2012). Upward sensible heat fluxes would promote more vigorous mixing by destabilizing the mixed layer but suppress the growth of liquid by increasing θ_{LM} . Upward latent heat fluxes would support liquid growth by increasing r_{vLM} and support more vigorous mixing by intensifying latent heating in updrafts. In the Arctic, downward sensible and latent heat fluxes are possible (Persson et al., 2002) and would have the opposite effects. However, these interactions would be weaker in the Arctic than in the midlatitudes because surface fluxes over sea ice are typically smaller (Persson et al., 2002).

The SCM simulations may help explain why r_v inversions are so frequently observed near the tops of Arctic stratocumuli (Sedlar et al., 2012; Sedlar & Tjernström, 2009). Thus far, two formation mechanisms for these r_v inversions have been proposed. First, the inversions may form through the detrainment of liquid water and water vapor at cloud top (Devasthale et al., 2011; Solomon et al., 2014). Second, they may form through differential advection of moisture near cloud top (Sedlar et al., 2012). The SCM simulations in this study suggest a third mechanism: That r_v inversions may form naturally when stratocumulus layers form. When a stratocumulus layer forms through clear-sky radiative cooling, the r_v decreases within the cloud layer as vapor condenses but does not decrease above the cloud top. This naturally produces a region in which the r_v increases with height and is similar to how cloud top r_v inversions formed in SCM simulations by Curry (1983).

Sensitivity tests with the SCM show that the properties of Arctic stratocumuli that form by radiative cooling are very sensitive to the properties of the environment in which the formation process takes place. For example, sensitivity tests show that clouds may attain LWPs of over 50 g/m^2 by simulation hour 10 if they form in moist environments but may become locked in a low-LWP quasi steady state or dissipate if they form in dry environments. The sensitivity tests also show that if cloud layers precipitate ice and form by radiative cooling when solar radiation is present, they are very likely to dissipate within hours after forming. Furthermore, the tests suggest that when stratocumuli form under lower static stability, they are more likely to dissipate if dry air is present above/below but may attain larger LWPs if dry air is absent. These sensitivities could have several important implications for the Arctic climate.

First, the sensitivities may help explain why the clear and cloudy radiative states are so prevalent across the Arctic. Figure 10a shows a contour plot of the downwelling longwave radiative flux at the surface, averaged between simulation hours 9 and 10, for all simulations in the SensMoisture set. Figure 10b shows the corresponding probability distribution for all longwave fluxes contoured in Figure 10a. Both panels show that the downwelling longwave fluxes cluster into two peaks, which correspond to the radiatively clear and opaquely cloudy states discussed by Shupe and Intrieri (2004) and Stramler et al. (2011). Corresponding plots (not shown) for the SensHiStability and SensLoStability sets show a similar bimodality. The bimodality implies that if an elevated Arctic stratocumulus cloud layer forms by radiative cooling, the column in which the cloud forms is afterward more likely to occupy one of the radiatively extreme states than an intermediate state. However, the extent to which this contributes to the prevalence of the clear and cloudy states in the Arctic cannot be assessed from these results. Such an assessment would require a more detailed treatment of microphysics and entrainment, as well as a realistic distribution of initial conditions and an accurate estimate of how frequently Arctic stratocumuli form in stable atmospheric layers.

Second, the simulations in the SensSZA80 and SensSZA70 sets suggest that solar radiation might inhibit the formation of persistent Arctic stratocumuli under certain conditions. Solar radiation is most likely to drive dissipation when conditions are sufficiently cold to support ice precipitation and when dry air is present in the surrounding atmosphere. These results contrast with observations from the NSA observatory, which show that liquid-containing clouds persist for longer in summer than during other seasons (Shupe et al., 2011). However, the observations do not necessarily discredit the modeling results because many of the observed cloud layers might have been too warm to produce ice or might have formed by other mechanisms.

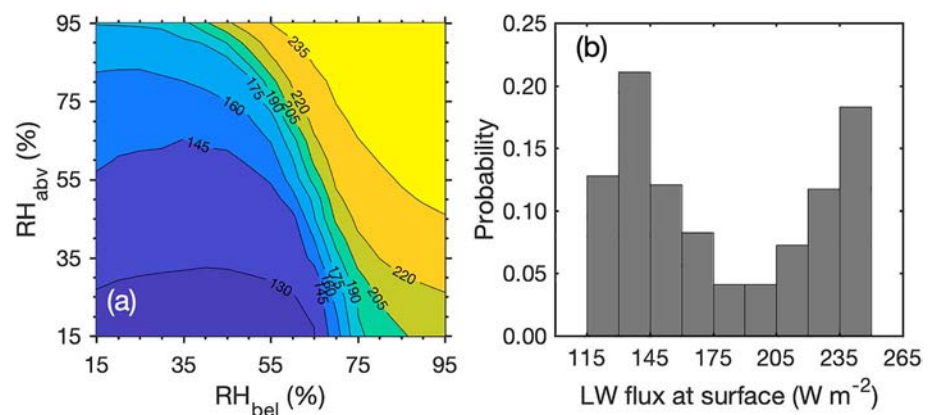


Figure 10. (a) Average downwelling LW radiation (W/m^2) at the surface between simulation hours 9 and 10, contoured as a function of the values of RH_{abv} and RH_{bel} used to initialize each simulation, for all simulations in the *SensMoisture* set. (b) Probability distribution for all LW fluxes plotted in (a). RH = relative humidity; LW = longwave.

Finally, the SCM simulations imply that changes in Arctic lower tropospheric static stability with global climate change may affect the properties of Arctic stratocumuli that form through radiative cooling. In regions where sea ice thickness or coverage decreases, static stability in the lower troposphere is likely to decrease as surface temperatures warm (Vihma, 2014). According to the simulations in the *SensLoStability* set, a decrease in static stability would reduce the number of persistent stratocumuli that form by radiative cooling but increase the average LWP of stratocumuli that do form by radiative cooling. Meanwhile, static stability might increase in regions where sea ice thickness or coverage does not decrease substantially, as warmer air advects into the Arctic. According to the simulations in the *SensHiStability* set, this would increase the number but decrease the LWPs of persistent stratocumuli that form by radiative cooling.

5. Conclusions

Radiative transfer calculations in this study suggest that clear-sky radiative cooling can drive the formation of Arctic stratocumulus clouds in stable atmospheric layers during all seasons. SCM simulations of the cloud formation process, after radiative cooling has led to saturation, are consistent with previous simulations of the formation process during summer. The simulations also put forth an explanation for why Arctic stratocumuli are able to persist despite their colloidal instability, which is consistent with previous work: That warming and drying through ice formation are too weak to outweigh liquid production through radiative cooling and the rising cloud top.

Large sets of sensitivity simulations suggest that the LWPs of cloud layers that form by radiative cooling are sensitive to the properties of the environment in which the formation process takes place. These sensitivities are qualitatively similar to the sensitivities of mature Arctic stratocumulus clouds but are especially severe because entrainment is much more rapid during the formation process than it is later in an Arctic stratocumulus cloud's lifetime. The strength of the sensitivities may have several important implications for the Arctic climate. For example, the sensitivity tests show that when an Arctic stratocumulus layer forms by clear-sky radiative cooling in the SCM, it is more likely to become optically thick, optically thin, or dissipate than it is to attain an intermediate optical thickness. It is possible that this contributes to the prevalence of cloudy and radiatively clear atmospheric states across the Arctic. However, it is important to emphasize that these sensitivities are closely linked to turbulent and microphysical processes, which our SCM does not accurately represent. Therefore, the sensitivities and their potential implications should be further investigated using more sophisticated modeling tools.

References

- Atmospheric Radiation Measurement (ARM) user facility (1990a). KAZR corrected data (KAZRCORGE). 2012-01-01 to 2015-12-31, North Slope Alaska (NSA) Central Facility, Barrow AK (C1), updated hourly. Compiled by A. Matthews, B. Isom, D. Nelson, I. Lindenmaier, J. Hardin, K. Johnson, N. Bharadwaj, S. Giangrande and T. Toto. ARM Data Center. Data set accessed 2016-09-28 at <https://doi.org/10.5439/1350632>

Acknowledgments

This research was supported by the U.S. Department of Energy's Atmospheric Science Program Atmospheric System Research, an Office of Science, Office of Biological and Environmental Research program, under Grant DE-SC0013953. The findings do not necessarily represent the views of the U.S. Department of Energy. This research was also supported by the NOAA Hollings Scholarship Program, which supported the lead author's early research at the NOAA Earth System Research Laboratory. LLNL work was performed under the auspices of the U.S. Department of Energy by Lawrence Livermore National Laboratory under Contract DE-AC52-07NA27344. All simulation output is available through DataCommons at Penn State, at their URL (<http://www.datacommons.psu.edu/commonswizard/MetadataDisplay.aspx?Dataset=6174>).

- Atmospheric Radiation Measurement (ARM) user facility (1990b). Cloud mask from micropulse lidar (30SMPLCMASK1ZWANG). 2012-01-01 to 2015-12-31, North Slope Alaska (NSA) Central Facility, Barrow AK (C1), updated hourly. Compiled by C. Sivaraman, K. Johnson, L. Riihimaki and S. Giangrande. ARM Data Center. Data set accessed 2016-09-28 at <https://doi.org/10.5439/1027736>
- Atmospheric Radiation Measurement (ARM) user facility (1993). Balloon-borne sounding system (SONDEWRPR). 2012-01-01 to 2015-12-31, North Slope Alaska (NSA) Central Facility, Barrow AK (C1), updated hourly. Compiled by C. Sivaraman, D. Holdridge, D. Troyan, J. Kyrouac, L. Riihimaki, R. Coulter, S. Giangrande, T. Shippert and T. Toto. ARM data center. Data set accessed 2016-09-28 at <https://doi.org/10.5439/1150271>
- Bechtold, P., Pinty, J. P., & Fravallo, C. (1992). A model of marine boundary-layer cloudiness for mesoscale applications. *Journal of the Atmospheric Sciences*, 49(18), 1723–1744. [https://doi.org/10.1175/1520-0469\(1992\)049<1723:AMOMBL>2.0.CO;2](https://doi.org/10.1175/1520-0469(1992)049<1723:AMOMBL>2.0.CO;2)
- Bennartz, R., Shupe, M. D., Turner, D. D., Walden, V. P., Steffen, K., Cox, C. J., et al. (2013). July 2012 Greenland melt extent enhanced by low-level liquid clouds. *Nature*, 496, 83–86. <https://doi.org/10.1038/nature12002>
- Brooks, I. M., Tjernström, M., Persson, P. O. G., Shupe, M. D., Atkinson, R. A., Canut, G., et al. (2017). The turbulent structure of the Arctic summer boundary layer during the Arctic Summer Cloud-Ocean Study. *Journal of Geophysical Research: Atmospheres*, 122, 9685–9704. <https://doi.org/10.1002/2017JD027234>
- Cohen, J., Screen, J. A., Furtado, J. C., Barlow, M., Whittleston, D., Coumou, D., et al. (2014). Recent Arctic amplification and extreme mid-latitude weather. *Nature Geoscience*, 7(9), 627–637. <https://doi.org/10.1038/ngeo2234>
- Cronin, T. W., & Tziperman, E. (2015). Low clouds suppress Arctic air formation and amplify high-latitude continental winter warming. *Proceedings of the National Academy of Sciences*, 112(37), 11,490–11,495. <https://doi.org/10.1073/pnas.1510937112>
- Curry, J. A. (1983). On the formation of continental polar air. *Journal of the Atmospheric Sciences*, 40(9), 2278–2292. [https://doi.org/10.1175/1520-0469\(1983\)040<2278:OTFOCP>2.0.CO;2](https://doi.org/10.1175/1520-0469(1983)040<2278:OTFOCP>2.0.CO;2)
- Curry, J. A. (1995). Interactions among aerosols, clouds, and climate of the Arctic Ocean. *Science of the Total Environment*, 160–161, 777–791. [https://doi.org/10.1016/0048-9697\(95\)04411-S](https://doi.org/10.1016/0048-9697(95)04411-S)
- Curry, J. A., Ebert, E. E., & Herman, G. F. (1988). Mean and turbulence structure of the summertime Arctic cloudy boundary layer. *Quarterly Journal of the Royal Meteorological Society*, 114(481), 715–746. <https://doi.org/10.1002/qj.49711448109>
- Curry, J. A., & Herman, G. F. (1985). Relationships between large-scale heat and moisture budgets and the occurrence of Arctic stratus clouds. *Monthly Weather Review*, 113(9), 1441–1457. [https://doi.org/10.1175/1520-0493\(1985\)113<1441:RBLSHA>2.0.CO;2](https://doi.org/10.1175/1520-0493(1985)113<1441:RBLSHA>2.0.CO;2)
- de Boer, G., Morrison, H., Shupe, M. D., & Hildner, R. (2011). Evidence of liquid dependent ice nucleation in high-latitude striform clouds from surface remote sensors. *Geophysical Research Letters*, 38, L01803. <https://doi.org/10.1029/2010GL046016>
- Deardorff, J. W. (1980). Cloud top entrainment instability. *Journal of the Atmospheric Sciences*, 37(1), 131–147. [https://doi.org/10.1175/1520-0469\(1980\)037<0131:CTEI>2.0.CO;2](https://doi.org/10.1175/1520-0469(1980)037<0131:CTEI>2.0.CO;2)
- Devasthale, A., Sedlar, J., & Tjernström, M. (2011). Characteristics of water-vapour inversions observed over the Arctic by Atmospheric Infrared Sounder (AIRS) and radiosondes. *Atmospheric Chemistry and Physics*, 11(18), 9813–9823. <https://doi.org/10.5194/acp-11-9813-2011>
- Garrett, T. J., Maestas, M. M., Krueger, S. K., & Schmidt, C. T. (2009). Acceleration by aerosol of a radiative-thermodynamic cloud feedback influencing Arctic surface warming. *Geophysical Research Letters*, 36, L19804. <https://doi.org/10.1029/2009GL040195>
- Golaz, J.-C. (1997). *Development of a single-column model for simulating precipitating stratocumulus clouds* (Master's thesis). Fort Collins, CO: Colorado State University.
- Gong, T., Feldstein, S., & Lee, S. (2017). The role of downward infrared radiation in the recent Arctic winter warming trend. *Journal of Climate*, 30(13), 4937–4949. <https://doi.org/10.1175/JCLI-D-16-0180.1>
- Harrington, J. Y. (1997). *The effects of radiative and microphysical processes on simulated warm and transition season Arctic stratus* (Doctoral dissertation). Fort Collins, CO: Colorado State University.
- Harrington, J. Y., & Olsson, P. Q. (2001a). On the potential influence of ice nuclei on surface-forced marine stratocumulus cloud dynamics. *Journal of Geophysical Research*, 106(D21), 27,473–27,484. <https://doi.org/10.1029/2000JD000236>
- Harrington, J. Y., & Olsson, P. Q. (2001b). A method for the parameterization of cloud optical properties in bulk and bin microphysical models: Implications for arctic cloudy boundary layers. *Atmospheric Research*, 57(1), 51–80. [https://doi.org/10.1016/S0169-8095\(00\)00068-5](https://doi.org/10.1016/S0169-8095(00)00068-5)
- Harrington, J. Y., Sulia, K., & Morrison, H. (2013). A method for adaptive habit prediction in bulk microphysical models. Part I: Theoretical development. *Journal of the Atmospheric Sciences*, 70(2), 349–364. <https://doi.org/10.1175/JAS-D-12-040.1>
- Herman, G., & Goody, R. (1976). Formation and persistence of summertime Arctic stratus clouds. *Journal of the Atmospheric Sciences*, 33(8), 1537–1553. [https://doi.org/10.1175/1520-0469\(1976\)033<1537:FAPOSA>2.0.CO;2](https://doi.org/10.1175/1520-0469(1976)033<1537:FAPOSA>2.0.CO;2)
- Intrieri, J. M., Fairall, C. W., Shupe, M. D., Persson, P. O. G., Andreas, E. L., Guest, P. S., & Moritz, R. E. (2002). An annual cycle of Arctic surface cloud forcing at SHEBA. *Journal of Geophysical Research*, 107(C10), 8039. <https://doi.org/10.1029/2000JC000439>
- Jensen, A. A., Harrington, J. Y., Morrison, H., & Milbrandt, J. A. (2017). Predicting ice shape evolution in a bulk microphysics model. *Journal of the Atmospheric Sciences*, 74(6), 2081–2104. <https://doi.org/10.1175/JAS-D-16-0350.1>
- Klein, S. A., McCoy, R. B., Morrison, H., Ackerman, A. S., Avramov, A., de Boer, G., et al. (2009). Intercomparison of model simulations of mixed-phase clouds observed during the ARM mixed-phase arctic cloud experiment. I: Single-layer cloud. *Quarterly Journal of the Royal Meteorological Society*, 135, 979–1002. <https://doi.org/10.1002/qj.416>
- Langland, R. H., & Liou, C.-S. (1996). Implementation of an E-ε parameterization of vertical subgrid-scale mixing in a regional model. *Monthly Weather Review*, 124(5), 905–918. [https://doi.org/10.1175/1520-0493\(1996\)124<0905:IOAPOV>2.0.CO;2](https://doi.org/10.1175/1520-0493(1996)124<0905:IOAPOV>2.0.CO;2)
- Larsen, J. N., Anisimov, O. A., Constable, A., Hollowed, A. B., Maynard, N., Prestrud, P., et al. (2014). Polar regions. In V. R. Barros, C. B. Field, D. J. Dokken, M. D. Mastrandrea, K. J. Mach, T. E. Bilir, M. Chatterjee, K. L. Ebi, Y. O. Estrada, R. C. Genova, B. Girma, E. S. Kissel, A. N. Levy, S. MacCracken, P. R. Mastrandrea, & L. L. White (Eds.), *Climate Change 2014: Impacts, Adaptation, and Vulnerability. Part B: Regional Aspects. Contribution of Working Group II to the Fifth Assessment Report of the Intergovernmental Panel on Climate Change* (pp. 1567–1612). Cambridge, UK and New York, NY: Cambridge University Press.
- Lee, S., Gong, T., Feldstein, S. B., Screen, J. A., & Simmonds, I. (2017). Revisiting the cause of the 1989–2009 Arctic surface warming using the surface energy budget: Downward infrared radiation dominates the surface fluxes. *Geophysical Research Letters*, 44, 10,654–10,661. <https://doi.org/10.1002/2017GL075375>
- Lu, J., & Cai, M. (2010). Quantifying contributions to polar warming amplification in an idealized coupled general circulation model. *Climate Dynamics*, 34(5), 669–687. <https://doi.org/10.1007/s00382-009-0673-x>
- McInnes, K. L., & Curry, J. A. (1995). *Lifecycles of summertime Arctic stratus clouds*. Presented at the Fourth Conference on Polar Meteorology and Oceanography, Dallas, TX: American Meteorological Society.
- Meyers, M. P., DeMott, P. J., & Cotton, W. R. (1992). New primary ice-nucleation parameterizations in an explicit cloud model. *Journal of Applied Meteorology*, 31(7), 708–721. [https://doi.org/10.1175/1520-0450\(1992\)031<0708:NPINPI>2.0.CO;2](https://doi.org/10.1175/1520-0450(1992)031<0708:NPINPI>2.0.CO;2)

- Mlawer, E. J., & Clough, S. A. (1997). On the extension of rapid radiative transfer model to the shortwave region. In *Proceedings of the 6th Atmospheric Radiation Measurement (ARM) Science Team Meeting* (pp. 223–226). U.S. Department of Energy.
- Mlawer, E. J., Taubman, S. J., Brown, P. D., Iacono, M. J., & Clough, S. A. (1997). Radiative transfer for inhomogeneous atmospheres: RRTM, a validated correlated-k model for the longwave. *Journal of Geophysical Research*, *102*(D14), 16,663–16,682. <https://doi.org/10.1029/97JD00237>
- Moritz, R. (2017). Soundings, Ice Camp NCAR/GLAS raobs. (ASCII). Version 2.0 [Data set]. UCAR/NCAR - Earth observing laboratory. <https://doi.org/10.5065/D6FQ9V0Z>
- Morrison, H., de Boer, G., Feingold, G., Harrington, J., Shupe, M. D., & Sulia, K. (2011). Resilience of persistent Arctic mixed-phase clouds. *Nature Geoscience*, *5*(1), 11–17. <https://doi.org/10.1038/ngeo1332>
- Morrison, H., Zuidema, P., Ackerman, A. S., Avramov, A., de Boer, G., Fan, J., et al. (2011). Intercomparison of cloud model simulations of Arctic mixed-phase boundary layer clouds observed during SHEBA/FIRE-ACE. *Journal of Advances in Modeling Earth Systems*, *3*, M06003. <https://doi.org/10.1029/2011MS000066>
- Nygård, T., Valkonen, T., & Vihma, T. (2014). Characteristics of Arctic low-tropospheric humidity inversions based on radio soundings. *Atmospheric Chemistry and Physics*, *14*(4), 1959–1971. <https://doi.org/10.5194/acp-14-1959-2014>
- Ovchinnikov, M., Ackerman, A. S., Avramov, A., Cheng, A., Fan, J., Fridlind, A. M., et al. (2014). Intercomparison of large-eddy simulations of Arctic mixed-phase clouds: Importance of ice size distribution assumptions. *Journal of Advances in Modeling Earth Systems*, *6*, 223–248. <https://doi.org/10.1002/2013MS000282>
- Ovchinnikov, M., Korolev, A., & Fan, J. (2011). Effects of ice number concentration on dynamics of a shallow mixed-phase stratiform cloud. *Journal of Geophysical Research*, *116*. <https://doi.org/10.1029/2011JD015888>
- Overland, J. E., Wang, M., Walsh, J. E., & Stroeve, J. C. (2014). Future Arctic climate changes: Adaptation and mitigation time scales. *Earth's Future*, *2*(2), 68–74. <https://doi.org/10.1002/2013EF000162>
- Persson, P. O. G., Fairall, C. W., Andreas, E. L., Guest, P. S., & Perovich, D. K. (2002). Measurements near the atmospheric surface flux group tower at SHEBA: Near-surface conditions and surface energy budget. *Journal of Geophysical Research*, *107*(C10), 8045. <https://doi.org/10.1029/2000JC000705>
- Pithan, F., Svensson, G., Caballero, R., Chechin, D., Cronin, T. W., Ekman, A. M. L., et al. (2018). Role of air-mass transformations in exchange between the Arctic and mid-latitudes. *Nature Geoscience*, *11*(11), 805–812. <https://doi.org/10.1038/s41561-018-0234-1>
- Randall, D. A. (1980). Conditional instability of the first kind upside-down. *Journal of the Atmospheric Sciences*, *37*(1), 125–130. [https://doi.org/10.1175/1520-0469\(1980\)037<0125:CIOTFK>2.0.CO;2](https://doi.org/10.1175/1520-0469(1980)037<0125:CIOTFK>2.0.CO;2)
- Sedlar, J., & Shupe, M. D. (2014). Characteristic nature of vertical motions observed in Arctic mixed-phase stratocumulus. *Atmospheric Chemistry and Physics*, *14*(7), 3461–3478. <https://doi.org/10.5194/acp-14-3461-2014>
- Sedlar, J., Shupe, M. D., & Tjernström, M. (2012). On the relationship between thermodynamic structure and cloud top, and its climate significance in the Arctic. *Journal of Climate*, *25*(7), 2374–2393. <https://doi.org/10.1175/JCLI-D-11-00186.1>
- Sedlar, J., & Tjernström, M. (2009). Stratiform cloud-inversion characterization during the Arctic melt season. *Boundary-Layer Meteorology*, *132*(3), 455–474. <https://doi.org/10.1007/s10546-009-9407-1>
- Shaw, G. E., & Stamnes, K. (1980). Arctic haze: Perturbation of the polar radiation budget. *Annals of the New York Academy of Sciences*, *338*(1 Aerosols), 533–539. <https://doi.org/10.1111/j.1749-6632.1980.tb17145.x>
- Shupe, M. D., & Intrieri, J. M. (2004). Cloud radiative forcing of the Arctic surface: The influence of cloud properties, surface albedo, and solar zenith angle. *Journal of Climate*, *17*(3), 616–628. [https://doi.org/10.1175/1520-0442\(2004\)017<0616:CRFOTA>2.0.CO;2](https://doi.org/10.1175/1520-0442(2004)017<0616:CRFOTA>2.0.CO;2)
- Shupe, M. D., Matrosov, S. Y., & Uttal, T. (2006). Arctic mixed-phase cloud properties derived from surface-based sensors at SHEBA. *Journal of the Atmospheric Sciences*, *63*(2), 697–711. <https://doi.org/10.1175/JAS3659.1>
- Shupe, M. D., Persson, P. O. G., Brooks, I. M., Tjernström, M., Sedlar, J., Mauritsen, T., et al. (2013). Cloud and boundary layer interactions over the Arctic sea ice in late summer. *Atmospheric Chemistry and Physics*, *13*(18), 9379–9399. <https://doi.org/10.5194/acp-13-9379-2013>
- Shupe, M. D., Walden, V. P., Eloranta, E., Uttal, T., Campbell, J. R., Starkweather, S. M., & Shiobara, M. (2011). Clouds at Arctic atmospheric observatories. Part I: Occurrence and macrophysical properties. *Journal of Applied Meteorology and Climatology*, *50*(3), 626–644. <https://doi.org/10.1175/2010JAMC2467.1>
- Solomon, A., Feingold, G., & Shupe, M. D. (2015). The role of ice nuclei recycling in the maintenance of cloud ice in Arctic mixed-phase stratocumulus. *Atmospheric Chemistry and Physics*, *15*(18), 10,631–10,643. <https://doi.org/10.5194/acp-15-10631-2015>
- Solomon, A., Shupe, M. D., Persson, O., Morrison, H., Yamaguchi, T., Caldwell, P. M., & de Boer, G. (2014). The sensitivity of springtime Arctic mixed-phase stratocumulus clouds to surface-layer and cloud-top inversion-layer moisture sources. *Journal of the Atmospheric Sciences*, *71*(2), 574–595. <https://doi.org/10.1175/JAS-D-13-0179.1>
- Sotiropoulou, G., Sedlar, J., Tjernström, M., Shupe, M. D., Brooks, I. M., & Persson, P. O. G. (2014). The thermodynamic structure of summer Arctic stratocumulus and the dynamic coupling to the surface. *Atmospheric Chemistry and Physics*, *14*(22), 12,573–12,592. <https://doi.org/10.5194/acp-14-12573-2014>
- Stepanyuk, O., Räisänen, J., Sinclair, V. A., & Järvinen, H. (2017). Factors affecting atmospheric vertical motions as analyzed with a generalized omega equation and the OpenIFS model. *Tellus A: Dynamic Meteorology and Oceanography*, *69*(1), 1271563. <https://doi.org/10.1080/16000870.2016.1271563>
- Stohl, A. (2006). Characteristics of atmospheric transport into the Arctic troposphere. *Journal of Geophysical Research*, *111*(D11). <https://doi.org/10.1029/2005JD006888>
- Stramler, K., Del Genio, A. D., & Rossow, W. B. (2011). Synoptically driven Arctic winter states. *Journal of Climate*, *24*(6), 1747–1762. <https://doi.org/10.1175/2010JCLI3817.1>
- Stull, R. B. (1988). *An introduction to boundary layer meteorology*. Dordrecht: Kluwer Academic Publishers. <https://doi.org/10.1007/978-94-009-3027-8>
- Sulia, K. J., Morrison, H., & Harrington, J. Y. (2014). Dynamical and microphysical evolution during mixed-phase cloud glaciation simulated using the bulk adaptive habit prediction model. *Journal of the Atmospheric Sciences*, *71*(11), 4158–4180. <https://doi.org/10.1175/JAS-D-14-0070.1>
- Tjernström, M., Shupe, M. D., Brooks, I. M., Persson, P. O. G., Prytherch, J., Salisbury, D. J., et al. (2015). Warm-air advection, air mass transformation and fog causes rapid ice melt. *Geophysical Research Letters*, *42*, 5594–5602. <https://doi.org/10.1002/2015GL064373>
- Valero, F. P. J., & Ackerman, T. P. (1985). *Arctic haze and the radiation balance* (No. NASA-TM-86784) (p. 30). Moffett Field, CA: NASA Ames Research Center.
- Vavrus, S. (2004). The impact of cloud feedbacks on Arctic climate under greenhouse forcing. *Journal of Climate*, *17*(3), 603–615. [https://doi.org/10.1175/1520-0442\(2004\)017<0603:TIOCFO>2.0.CO;2](https://doi.org/10.1175/1520-0442(2004)017<0603:TIOCFO>2.0.CO;2)

- Vihma, T. (2014). Effects of Arctic sea ice decline on weather and climate: A review. *Surveys in Geophysics*, 35(5), 1175–1214. <https://doi.org/10.1007/s10712-014-9284-0>
- Walko, R. L., Cotton, W. R., Meyers, M. P., & Harrington, J. Y. (1995). New RAMS cloud microphysics parameterization part I: The single-moment scheme. *Atmospheric Research*, 38(1–4), 29–62. [https://doi.org/10.1016/0169-8095\(94\)00087-T](https://doi.org/10.1016/0169-8095(94)00087-T)
- Wang, Z., & Sassen, K. (2001). Cloud type and macrophysical property retrieval using multiple remote sensors. *Journal of Applied Meteorology*, 40(10), 1665–1682. [https://doi.org/10.1175/1520-0450\(2001\)040<1665:CTAMPR>2.0.CO;2](https://doi.org/10.1175/1520-0450(2001)040<1665:CTAMPR>2.0.CO;2)
- Wilson, W. H. (1980). *Solar ephemeris algorithm* (No. SIO Ref. 80-13) (p. 70). La Jolla, CA: Scripps Institution of Oceanography.
- Young, G., Connolly, P. J., Dearden, C., & Choularton, T. W. (2018). Relating large-scale subsidence to convection development in Arctic mixed-phase marine stratocumulus. *Atmospheric Chemistry and Physics*, 18(3), 1475–1494. <https://doi.org/10.5194/acp-18-1475-2018>
- Zhang, Q. (1999). *Modeling of Arctic stratus cloud formation and the maintenance of the cloudy Arctic boundary layer* (Doctoral dissertation). Fairbanks, AK: University of Alaska Fairbanks.